Acta Pharmaceutica Sinica B 2026;16(6):3680−3697

Chinese Pharmaceutical Association
Institute of Materia Medica, Chinese Academy of Medical Sciences

Acta Pharmaceutica Sinica B

www.elsevier.com/locate/apsb
www.sciencedirect.com

ORIGINAL ARTICLE

Syringin disrupts the DLAT/MYC axis to dampen TAM polarization and suppress hepatocellular carcinoma progression

Lingyun Xiao[a,†], Jiawei Lv[a,†], Yuan Lu[b,†], Zun Li[a], Liang-Mei Yang[b], Zheng Li[a], Shu Liang[a,*], Ke-Bin Huang[b,*], Xiongjun Wang[a,c,*]

[a]*Precise Genome Engineering Center, School of Life Sciences, Guangzhou University, Guangzhou 510006, China*
[b]*Key Laboratory for Chemistry and Molecular Engineering of Medicinal Resources (Ministry of Education of China), Guangxi Key Laboratory of Chemistry and Molecular Engineering of Medicinal Resources, School of Chemistry and Pharmaceutical Sciences, Guangxi Normal University, Guilin 541004, China*
[c]*Department of Laboratory Medicine, Shanghai Tenth People's Hospital of Tongji University, Shanghai 200072, China*

Received 30 June 2025; received in revised form 7 November 2025; accepted 14 January 2026

KEY WORDS

Hepatocellular carcinoma (HCC);
Tumor-associated macrophages (TAMs);
Macrophage polarization;
Dihydrolipoamide *S*-acetyltransferase (DLAT);
MYC degradation;
Syringin;
Single-cell RNA sequencing (scRNA-seq)

Abstract Tumor-associated macrophages (TAMs) are pivotal drivers of hepatocellular carcinoma (HCC) progression, and blocking TAM M2 polarization has the potential to dampen tumor microenvironment remodeling. In this study, we screened a series of phenylethanoid and phenylpropanoid glycosides and identified syringin as a natural compound capable of inhibiting M2 polarization while promoting M1 polarization in macrophages. Single-cell RNA sequencing confirmed that syringin reduced TAM M2 polarization and significantly impaired tumor microenvironment remodeling. In detail, syringin indirectly reduced the stability of MYC proto-oncogene protein (MYC), which is required for driving a broad set of targets, including *Arg1*, *Il10*, *Ym1*, *Mrc1*, and *Cd274*. Using affinity-based protein profiling (ABPP), we revealed dihydrolipoamide *S*-acetyltransferase (DLAT) as a direct target of syringin. DLAT possesses protein acetyltransferase activity that acetylates MYC at K148. Syringin bound DLAT at residues R430 and N576 and disrupted the DLAT/MYC axis, thereby blocking MYC acetylation and promoting the ubiquitination and degradation of MYC protein. Additionally, syringin enhanced the efficacy of programmed cell death protein 1 blockade in mouse and patient-derived xenograft models, offering a potential adjunctive agent for HCC.

*Corresponding authors.
E-mail addresses: liangshu@gzhu.edu.cn (Shu Liang), kbhuang@mailbox.gxnu.edu.cn (Ke-Bin Huang), wangxiongjun@gzhu.edu.cn (Xiongjun Wang).
[†]These authors made equal contributions to this work.
Peer review under the responsibility of Chinese Pharmaceutical Association and Institute of Materia Medica, Chinese Academy of Medical Sciences.

https://doi.org/10.1016/j.apsb.2026.03.036

Tumor microenvironment (TME)

1. Introduction

Hepatocellular carcinoma (HCC) accounts for approximately 75%−85% of primary liver cancers, ranking as the sixth most common cancer worldwide and the fourth leading cause of cancer-related mortality[1]. Characterized by a subtle onset and aggressive progression, HCC presents profound therapeutic challenges. Despite advancements in treatments, including tyrosine kinase inhibitors and vascular endothelial growth factor receptor 2-targeting agents such as ramucirumab, the prognosis for most HCC patients remains grim, with a 5-year survival rate ranging from 15% to 40%[2].

One key reason for the suboptimal efficacy of cancer therapies is the tumor microenvironment (TME), which provides a supportive milieu for tumor progression. HCC is associated with a highly immunosuppressive TME, and several immune checkpoint blockers (ICBs) have been incorporated into therapeutic regimens for advanced HCC[3]. For instance, the combination of the programmed death-ligand 1 (PD-L1) antibody atezolizumab with the anti-angiogenic agent bevacizumab has been established as a first-line therapy for advanced or unresectable HCC[4]. However, while atezolizumab and other programmed cell death protein 1 (PD-1)/PD-L1-targeting agents have been approved, their survival benefits remain limited, underscoring the need for novel treatment strategies.

Tumor-associated macrophages (TAMs) constitute a major immunosuppressive compartment within the TME[5,6]. TAMs exhibit heterogeneity, with lipopolysaccharide (LPS) or interferon gamma (IFN-γ) promoting an M1-like phenotype (pro-inflammatory, antitumor), whereas interleukin 4 (IL-4) or interleukin 13 (IL-13) promotes an M2-like phenotype (anti-inflammatory, protumor)[7]. In the TME, TAMs predominantly adopt an M2-like phenotype, secreting cytokines such as interleukin 10 (IL-10) and transforming growth factor beta (TGF-β) and expressing immune checkpoints like PD-L1. TAMs contribute to various aspects of HCC progression, including cancer stemness, epithelial-to-mesenchymal transition, angiogenesis, and the suppression of $CD8^+$ T cell activity[8]. Strategies targeting TAMs, such as colony-stimulating factor 1/colony-stimulating factor 1 receptor (CSF1/CSF1R) and chemokine (C−C motif) ligand 2/chemokine (C−C motif) receptor 2 (CCL2/CCR2) blockade, show therapeutic potential but face limitations owing to the inadvertent depletion of tissue-resident macrophages, thereby limiting their application in advanced tumors[9-11].

Modulating TAM polarization represents a promising strategy to inhibit tumor progression[12]. In our previous study, we demonstrated that phenylethanoid and phenylpropanoid glycosides have the potential to modulate macrophage polarization[13]. Among the 49 isolated glycosides, most were found to impair the expression of inducible nitric oxide synthase (iNOS) or directly reduce nitric oxide (NO) levels upregulated by LPS and IFN-γ. However, a few compounds, such as syringin, were shown to enhance NO levels[13]. Building upon these findings, the current study further investigates the modulation of macrophage M2 polarization by these phenylethanoid and phenylpropanoid glycosides, aiming to identify potential candidates for treating HCC.

2. Materials and methods

2.1. Reagents

Syringin (purity >98%) was purchased from Macklin (Shanghai, China). LPS (*Escherichia coli* O55:B5) was obtained from Sigma (St. Louis, MO, USA). Murine IL-4, IL-13, IFN-γ, and macrophage colony-stimulating factor (M-CSF) were purchased from Novoprotein (Shanghai, China). Murine isotype controls, anti-CSF1R (clone: AFS98), and anti-PD-1 antibodies (clones: RMP1-14 and J116) were purchased from Bio X cell (West Lebanon, USA). Information on other antibodies is listed in Supporting Information Table S1. Cycloheximide (CHX) and MG132 were purchased from Selleckchem. D-Luciferin potassium salt was purchased from Beyotime. All chemicals were purchased from Sigma, unless otherwise stated.

2.2. Cell culture

The HCC cell lines Hepa1-6 and Hep3B, as well as the THP-1 cell line, were obtained from the American Type Culture Collection (ATCC). iBMDMs were from OriCell (Guangzhou, China). All cell lines except THP-1 were maintained in Dulbecco's modified Eagle's medium (DMEM) supplemented with 10% fetal bovine serum (FBS) and 1% penicillin/streptomycin at 37 °C in 5% CO_2, and were routinely tested and confirmed to be mycoplasma-negative. Luciferase was expressed in Hepa1-6 cells *via* lentiviral transduction, and stable positive clones were selected by antibiotic selection.

Primary bone marrow-derived monocytes were isolated from femurs and tibias of C57BL/6 mice. After centrifugation at $500\times g$, the cells were cultured in DMEM supplemented with 10% FBS, 1% penicillin/streptomycin, and 100 ng/mL murine M-CSF for 6 days to generate bone marrow-derived macrophages (BMDMs). The medium was refreshed every 3 days to remove non-adherent cells. To induce M1 polarization, BMDMs were treated with 10 ng/mL LPS and 20 ng/mL IFN-γ for 24 h, while 20 ng/mL IL-4 was used for M2 polarization. For co-culture experiments, 1×10^6 BMDMs were seeded in six-well plates and co-cultured with 2×10^6 Hepa1-6 cells, which had been pre-cultured in inserts for 12 h. After 48 h of co-culture, the cells and culture supernatants were collected for subsequent analysis.

THP-1 cells were cultured in Roswell Park Memorial Institute 1640 medium (RPMI 1640) supplemented with 10% FBS, 1% penicillin/streptomycin, and 2 mmol/L L-glutamine. To differentiate THP-1 monocytes into macrophages, cells were treated with 150 nmol/L phorbol 12-myristate 13-acetate (PMA) for 72 h, followed by 24 h incubation in fresh culture medium to allow the cells to return to a resting state. For M2 polarization, differentiated THP-1 macrophages were stimulated with 20 ng/mL IL-4 and 20 ng/mL IL-13 for 48 h.

2.3. Overexpression, knockdown, and CRISPR/Cas9-mediated knockout

The mouse *Myc* gene (Myc proto-oncogene, bHLH transcription factor) was PCR-amplified and cloned into the pCDH-CMV-

MCS-EF1-BSD or the pLVX-3 × Flag-MCS-IRES-Puro vector. The GST sequence was amplified from the pGEX-6P-3 vector, and the GST-Myc fusion construct was generated using overlap extension PCR, followed by insertion into the pCDH-CMV-MCS-EF1-BSD vector. Similarly, the mouse *Dlat* gene (dihydrolipoamide S-acetyltransferase) was PCR-amplified and cloned into the pLVX-3 × Flag-MCS-IRES-Puro vector. Site-directed mutagenesis was performed using a Q5 mutagenesis kit (New England Biolabs, Ipswich, USA) to generate the following mutations: MYC p.K148R, DLAT p.R430A, and DLAT p.N576K, as well as shRNA-resistant MYC and DLAT. For knockdown experiments, shRNA target sequences were designed and cloned into the pLKO.1 vector (Supporting Information Table S2). shRNA-resistant MYC and DLAT were generated by introducing silent nucleotide mutations within the shRNA-targeting sequences. Details are shown in Table S2.

For CRISPR/Cas9-mediated knockout, a lentiviral CRISPR/Cas9 system was employed to generate DLAT-knockout iBMDMs, as reported previously[14]. The gRNA for DLAT knockout was designed using CRISPOR (https://crispor.tefor.net/) (Table S2). The gRNA was cloned into the LentiCRISPRv2 vector, and lentivirus was produced for transduction. Transduced iBMDMs were selected, and single-cell clones were isolated by limiting dilution. Control cells were generated by transducing iBMDMs with an empty LentiCRISPRv2 vector. Knockout efficiency was confirmed by Western blot analysis. Subsequently, DLAT wild-type (WT) and the double mutant DLAT R430A + N576K were separately expressed in DLAT knockout iBMDMs *via* lentiviral transduction.

2.4. Murine HCC model

All animal experiments were conducted in accordance with protocols approved by the Animal Ethics Committee of Guangzhou University (approval No. 2024-25). Myeloid-specific *Myc* knockout mice ($Lyz2^{+}Myc^{f/f}$) were generated by crossing $Myc^{f/f}$ mice with *Lyz2*-Cre mice, and $Myc^{f/f}$ mice were used as controls. All mice were housed under a 12 h light/12 h dark cycle with *ad libitum* access to food and water.

For the orthotopic HCC model, 3×10^6 Hepa1-6 cells were injected into the subcapsular region of the left liver lobe of 6-week-old male mice. Treatments, including syringin (40 mg/kg), anti-PD-1 antibody (αPD-1; 250 μg per mouse), anti-CSF1R antibody (αCSF1R; 200 μg per mouse), or isotype control, were administered *via* intraperitoneal injection. For bioluminescence imaging, mice were anesthetized with isoflurane and intraperitoneally injected with 150 mg/kg D-luciferin 10 min prior to imaging.

For the subcutaneous HCC model, 5×10^6 Hepa1-6 cells suspended in 100 μL PBS were injected into the right flanks of 6-week-old male mice. Tumor volume was measured every 3 days using vernier calipers, with length (L) and width (W) used to calculate volume (V) as Eq. (1):

$$V = 0.52 \times (L \times W^2) \quad (1)$$

The plasmids for Sleeping Beauty (SB) transposon-driven hepatocarcinogenesis, including pT3-EF1a-MET, pT3-EF1a-CTNNB1-S45Y, and pCMV-SB13, were kindly provided by Professor Lijian Hui. The oncogene-expressing constructs were delivered into 6-week-old male mice *via* hydrodynamic tail-vein injection, as described previously[15]. Liver tumors induced by the SB transposon system typically develop within 6−8 weeks.

All clinical samples were collected from Shanghai Tenth People's Hospital with the approval No. 23KN167 of the ethics committees and the written consent of each participant. For patient-derived xenograft (PDX) transplantation, fresh tumor fragments were collected from HCC patients and prepared to a uniform size of 3 mm × 3 mm × 3 mm. Peripheral blood mononuclear cells (PBMCs) from the same patients were isolated and expanded *in vitro* for subsequent use. 6-week-old NSG mice were pretreated to induce myeloablation. Briefly, mice received intraperitoneal injections of cyclophosphamide at 150 mg/kg. Concurrently, disulfiram was administered intragastrically at 125 mg/kg in 0.8% tween-80 saline solution daily for two consecutive days. Disulfiram treatment was initiated 2 h after cyclophosphamide administration to ensure optimal preconditioning. Then, tumor fragments were subcutaneously implanted into the mice. After wound healing, 200 μL of 5×10^6 PBMCs were administered subcutaneously in the right flank of the mice. After tumor establishment on Day 6, mice were treated with syringin (40 mg/kg) every 2 days, either alone or in combination with anti-human PD-1 antibody (250 μg per mouse) every 3 days. Tumor volume was assessed every 3 days as described above.

2.5. Single-cell RNA sequencing

Fresh tumors from three mice per group were harvested and pooled, then dissociated using 1 mg/mL collagenase and 0.1 mg/mL DNase I with a gentleMACS Dissociator (Miltenyi Biotec, Bergisch Gladbach, Germany) to generate a single-cell suspension. Cells were resuspended at a concentration of 1×10^6 cells/mL, and samples with viability exceeding 95% were used for library preparation. Library preparation followed the standard protocol provided by the 10x Genomics platform. Library quantification and quality assessment were performed using a DNA 1000 chip (Agilent Technologies, Santa Clara, USA), and samples were subsequently diluted and loaded onto the HiSeq 4000 (Illumina, San Diego, USA) for sequencing. Raw sequencing data were processed using Cell Ranger (v2.0) for demultiplexing, barcode processing, sequence alignment, filtering, and UMI counting. The resulting count data were analyzed in R (v4.2.1) using the Seurat package (v4.2.0) for downstream analysis and annotation. Batch effects were corrected using Harmony (v0.1.0), followed by data normalization in Seurat. Principal component analysis was performed on the top 2000 variable genes to identify cell clusters. Clustering results were visualized using uniform manifold approximation and projection (UMAP), and cell types were annotated with the SingleR package. Cell−cell interactions were analyzed using the CellChat package (v1.6.0). All visualizations were generated in R using the ggplot2 package. Macrophages in the single-cell RNA sequencing (scRNA-seq) dataset were subclustered and analyzed using Seurat AddModuleScore[16,17] with M1 and M2 gene signatures listed in Supporting Information Table S3.

2.6. qPCR, ChIP-qPCR, immunofluorescence, immunoblotting, and ELISA

Total RNA isolation, cDNA synthesis, and qPCR analysis were performed as previously described[18]. ChIP-qPCR was also performed with IgG or anti-MYC antibody as described[19]. Primer pairs used for qPCR and ChIP-qPCR[20,21] are listed in Supporting Information Table S4. Antibodies used for immunoprecipitation and Western blotting are listed in Table S1. Notably, antibodies

were used at 1:1000 for Western blot, 5 μg per sample for immunoprecipitation, and 1:100-1:200 for immunofluorescence. For immunofluorescence staining of surface proteins such as CD206 and PD-L1, cells were fixed with 4% paraformaldehyde and subjected to a non-permeabilized surface-staining procedure using primary antibodies, followed by Alexa Fluor-conjugated secondary antibodies and 4′,6-diamidino-2-phenylindole (DAPI) counterstaining. Enrichment of ubiquitinated proteins was performed using pan-selective TUBE2 agarose (#UM402, LifeSensor, Malvern, USA) as described[22,23]. Secreted IL-10 in cell supernatants was quantified by ELISA (E-HSEL-M0004, Elabscience, Wuhan, China) following the manufacturer's instructions.

2.7. Flow cytometry

Isolated tumor tissues were minced into small pieces and digested with 1 mg/mL collagenase and 0.1 mg/mL DNase I using a gentleMACS Dissociator. Fc receptors were blocked with anti-mouse CD16/32 antibodies, and cells were stained with fluorochrome-conjugated antibodies against surface markers. For intracellular staining, cells were fixed and permeabilized using a Foxp3/Transcription Factor Fixation/Permeabilization kit (eBioscience, San Diego, CA), then incubated with antibodies targeting intracellular markers. Flow cytometry was performed on a FACSAria III platform (BD Biosciences, San Jose, USA), and data were analyzed using FlowJo software.

2.8. Multiplex immunofluorescence

The multiplexed immunofluorescence assay was performed using the Opal 7-Color Manual IHC Kit (Akoya Biosciences, Marlborough, USA) as described previously[24]. Briefly, the formalin-fixed, paraffin-embedded tumor sections (4−5 μm) were deparaffinized, rehydrated, and subjected to antigen retrieval using an AR6 or AR9 buffer for 15 min in a microwave. Staining followed the Opal workflow in sequential cycles consisting of primary antibody incubation, HRP-polymer secondary antibody detection, and tyramide signal amplification with Opal-520/570/650 (1:100−1:150), followed by a brief heat-induced epitope retrieval step to strip antibodies while retaining the deposited fluorophores before the next cycle. Nuclei were counterstained with DAPI, and slides were mounted. Images were acquired under identical exposure and gain settings for each group ($n = 5$ mice).

2.9. Molecular docking

The murine DLAT structure was predicted using AlphaFold3. The receptor protein was prepared by adding hydrogen atoms and assigning Gasteiger charges using AutoDockTools, and both the receptor protein and ligand molecule were converted to the PDBQT format. Molecular docking was performed with AutoDock Vina 1.1.2, and the results were analyzed with Protein−Ligand Interaction Profiler. Visualization of the docking results was performed in PyMOL. The docking output is provided as a supplementary file.

2.10. Biolayer interferometry

Biolayer interferometry (BLI) experiments were performed at 30 °C using a Gator bio-layer interferometry system (Gator Bio, Palo Alto, USA). Reagents and samples were equilibrated to room temperature before testing. Kinetics buffer (PBS with 0.05% tween-20 and 0.1% bovine serum albumin) was used to minimize nonspecific binding. Proteins were immobilized on SMAP biosensors, following the manufacturer's instructions. Biosensors were hydrated in the kinetics buffer for 10 min, and proteins were loaded at 15 μg/mL for 800 s. The association phase was monitored by exposing the sensors to analytes at serial concentrations for 120 s, followed by a 120-s dissociation phase in kinetics buffer. Each concentration was tested in duplicate. Binding kinetics data were analyzed using Octet Data Analysis software to calculate association rate constant (K_{on}), dissociation rate constant (K_{off}), and equilibrium dissociation constant (K_d). Negative controls with reference sensors were included to account for nonspecific binding, and only data with $R^2 > 0.95$ were retained for further analysis.

2.11. Cellular thermal shift assay

Cells were treated with 100 μmol/L syringin or PBS and incubated at 37 °C for 3 h. After treatment, cells were harvested, washed with PBS, and resuspended in PBS supplemented with protease inhibitors. The cell suspension was subjected to three freeze−thaw cycles, alternating immersion in liquid nitrogen and thawing at room temperature, to ensure complete cell lysis. The lysate was aliquoted and heated across a temperature gradient for 3 min, then cooled on ice for 3 min. Samples were then centrifuged at 20,000×g for 20 min at 4 °C to separate soluble proteins from aggregates. The supernatant, containing soluble proteins, was analyzed by SDS-PAGE and Western blotting to detect the target protein.

2.12. LC−MS/MS-based targets identification

The syringin probe (syringin-p; compound **5′**) was synthesized as follows: 1) A solution of compound **1′** (10.3 g, 45.9 mmol) and *p*-toluenesulfonic acid (0.79 g, 4.6 mmol) in ethanol (100 mL) was heated at 75 °C for 20 h. After cooling to room temperature, the solvent was removed under reduced pressure. The residue was dissolved in ethyl acetate (200 mL) and washed successively with 5% aqueous Na_2CO_3 and brine. The organic phase was concentrated under vacuum, and the crude product was recrystallized from an ethyl acetate/*n*-hexane mixture ($v/v = 1:10$) to afford compound **2′** as a white solid. 2) Compound **2′** (500 mg, 1.98 mmol) was dissolved in $CHCl_3$ (10 mL), followed by the addition of 20% aqueous K_2CO_3 (6 mL) and tetrabutylammonium bromide (TBAB) (639 mg, 1.98 mmol). The mixture was stirred vigorously at room temperature for 10 min. Acetobromo-α-D-glucose (978 mg, 2.38 mmol) was then added, and the reaction mixture was heated to 65 °C and stirred for an additional 2 h. After cooling to room temperature, the mixture was diluted with $CHCl_3$ (20 mL). The organic layer was washed with brine, dried over anhydrous Na_2SO_4, and concentrated under reduced pressure. The residue was purified by silica gel column chromatography (ethyl acetate/petroleum ether = 1:2) to afford compound **3′**. 3) Compound **3′** (600 mg, 1 mmol) was dissolved in ethanol (10 mL), and 1 mol/L aqueous NaOH (10 mL) was added. The resulting suspension was stirred at room temperature for 4 h. After the reaction was complete, ethanol (40 mL) was added, and the mixture was cooled to 0 °C in an ice bath and neutralized to pH 4.0−4.5 by adding Amberlite IR-120. The product was eluted from the resin with ethanol, and the eluate was concentrated under reduced pressure to afford compound **4′**. (4) Compound **4′**

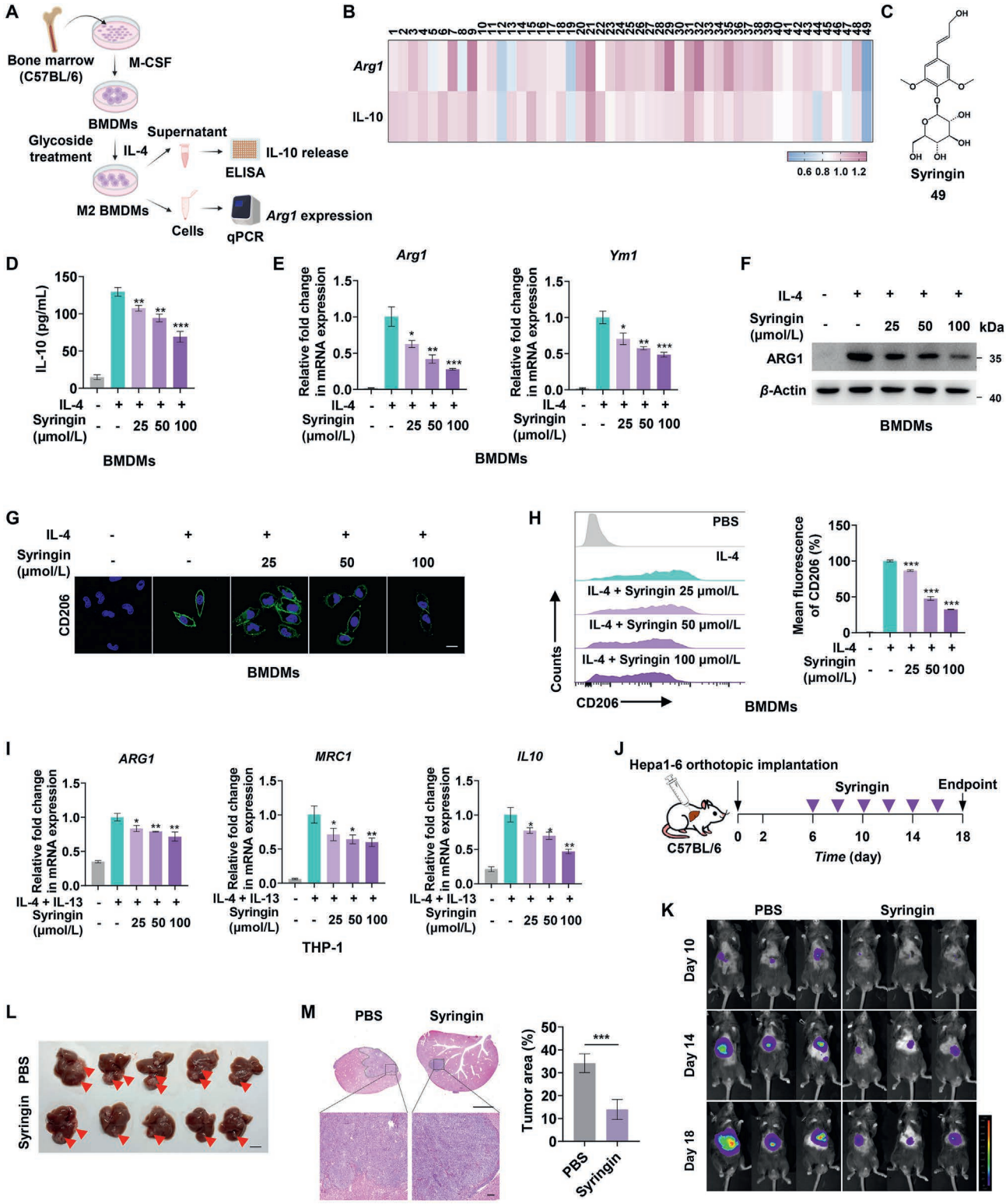

Figure 1 Syringin, a natural phenylpropanoid glycoside, regulates macrophage polarization and suppresses hepatocellular carcinoma (HCC). (A) Bone marrow-derived macrophages (BMDMs) from C57BL/6 mice were used to screen phenylethanoid/phenylpropanoid glycosides for their ability to inhibit M2 polarization. BMDMs were differentiated with 100 ng/mL macrophage colony-stimulating factor (M-CSF) for 6 days and then co-treated with IL-4 (20 ng/mL) and a glycoside (100 μmol/L) for 24 h. (B) Effects of each compound on *Arg1* mRNA expression and IL-10 secretion in IL-4-polarized BMDMs. Syringin (Compound **49**) emerged as the top hit. (C) Chemical structure of syringin. (D) Syringin suppressed IL-10 secretion in supernatants from IL-4-polarized BMDMs. (E) Syringin reduced *Arg1* and *Ym1* mRNA in IL-4-treated BMDMs. (F) Syringin decreased ARG1 protein in IL-4-treated BMDMs. (G, H) Immunofluorescence (G) and flow cytometry (H) showed reduced CD206 in IL-4-polarized BMDMs. Scale bar: 10 μm. Statistical comparisons were performed against the IL-4 group. (I) In THP-1 cells polarized with IL-

(500 mg, 1.29 mmol) was dissolved in *N*,*N*-dimethylformamide (DMF) (10 mL) and stirred at room temperature for 10 min. *O*-(7-Azabenzotriazol-1-yl)-*N*,*N*,*N*′,*N*′-tetramethyluronium hexafluorophosphate (HATU) (738 mg, 1.94 mmol) was added, followed by *N*,*N*-diisopropylethylamine (DIPEA) (508 mg, 3.88 mmol). After 20 min, a solution of Azido-PEG2-amine (225 mg, 1.29 mmol) in DMF (3 mL) was added dropwise, and the reaction mixture was stirred at room temperature for 12 h. The progress of the reaction was monitored by thin-layer chromatography. The mixture was then diluted with ethyl acetate, washed with brine, dried over anhydrous Na_2SO_4, and concentrated under reduced pressure. The crude product was purified by semi-preparative reverse-phase high-performance liquid chromatography on a C_{18} column (Cosmosil 5C18-MS-II, 10 mm × 250 mm, 5 μm) using 20% acetonitrile in water as the mobile phase to afford compound **5′** (syringin-p). M2 polarized BMDMs were treated with or without 100 μmol/L syringin for 1 h, and then incubated with 20 μmol/L syringin-p for 3 h. After cell lysis, 60 μmol/L DBCO-PEG3-biotin was added to the lysate, enabling covalent coupling of syringin-p *via* a click reaction. Target proteins were isolated using streptavidin beads, followed by silver staining and LC−MS/MS analysis. The mass spectrometry results identifying targets are shown in Supporting Information Table S5.

2.13. Recombinant proteins

Plasmids encoding GST-MYC, GST-MYC K148R, Flag-DLAT WT, Flag-DLAT-t1 (1-529), Flag-DLAT-t2 (1-499), Flag-DLAT-t3 (1-411), Flag-DLAT R430A, Flag-DLAT N576K, or Flag-DLAT R430A + N576K were transfected into HEK293T cells for 72 h. Recombinant proteins were purified from cell lysates using immunoprecipitation with anti-GST or anti-FLAG agarose beads.

2.14. In vitro acetylation assay

The *in vitro* acetylation assay was performed as described previously[25]. Purified GST-MYC WT or GST-MYC K148R was incubated with or without Flag-DLAT WT, Flag-DLAT R430A, Flag-DLAT N576K, or Flag-DLAT R430A + N576K in 30 μL of reaction buffer (20 mmol/L Tris-HCl, pH 8.0, 20% glycerol, 100 mmol/L KCl, 1 mmol/L dithiothreitol, 0.2 mmol/L ethylenediaminetetraacetic acid, 10 mmol/L trichostatin A, 10 mmol/L nicotinamide, and 100 mmol/L acetyl-CoA) at 30 °C for 1 h. The reaction was stopped by adding SDS-PAGE loading buffer and heating at 95 °C for 10 min. The samples were then subjected to Western blot analysis.

2.15. Statistical analysis

All data were analyzed using GraphPad Prism 9 and are presented as mean ± standard deviation (SD), as indicated in the figure legends. Comparisons between two independent groups were performed using a two-tailed Student's *t*-test. Multiple-group comparisons were performed using one-way or two-way ANOVA with Tukey's HSD *post hoc* test. For survival analyses, Kaplan−Meier survival curves were generated, and statistical differences were evaluated using the log-rank (Mantel-Cox) test. Statistical significance is indicated as follows: $*P < 0.05$, $**P < 0.01$, $***P < 0.001$.

3. Results

3.1. The phenylpropanoid glycoside syringin inhibits macrophage M2 polarization and impairs HCC progression

The capacity of 49 phenylethanoid and phenylpropanoid glycosides to modulate M2 polarization was assessed in IL-4-stimulated BMDMs, with *Arg1* expression and IL-10 release as screening markers (Fig. 1A). Initial screening revealed that syringin (compound **49**) exhibited the most potent inhibition of both *Arg1* mRNA expression and IL-10 release among the tested compounds (Fig. 1B). The chemical structure of syringin is shown in Fig. 1C. Further validation experiments demonstrated that syringin dose-dependently suppressed the expression of *Arg1* and *Ym1* genes, as well as ARG1 protein expression and IL-10 release (Fig. 1D−F). Consistent with these findings, syringin significantly reduced CD206 expression in BMDMs, a key marker of the M2 phenotype (Fig. 1G and H). Syringin also exhibited similar inhibitory effects on M2 polarization induced by Hepa1-6 co-culture, as indicated by the downregulation of *Arg1*, *Mrc1* (encoding CD206), and *Il10* mRNA expression (Supporting Information Fig. S1A). Furthermore, syringin significantly suppressed *ARG1*, *MRC1*, and *IL10* mRNA levels in IL-4 and IL-13-induced THP-1 M2 polarization (Fig. 1I).

Regarding M1 polarization, syringin dose-dependently increased iNOS expression and the phosphorylation of nuclear factor κB (NF-κB) p65, accompanied by elevated expression of M1-associated genes (*Il1b* and *Il6*) in LPS and IFN-γ-stimulated BMDMs (Fig. S1B and S1C). It also enhanced CD86 expression in BMDMs, further supporting its role in M1 macrophage activation (Fig. S1D). These findings are consistent with a previous report demonstrating syringin's ability to enhance NO release[13].

In vitro experiments showed that syringin had minimal effects on Hepa1-6 cell proliferation, migration, or colony formation at low concentrations, with only slight growth inhibition observed at 200 μmol/L after 48 h of treatment (Fig. S1E−S1G). Similar results were obtained in HCC cell lines, Hep-53.4 and Hep3B, where modest inhibition of proliferation and colony formation was evident only at high concentrations (Fig. S1H−S1M). The antitumor activity of syringin was assessed in an orthotopic HCC model (Fig. 1J). *In vivo* imaging performed on Day 10, 4 days after syringin treatment, revealed significantly reduced tumor growth, with an even more pronounced effect observed on Day 18 (Fig. 1K). Consistent with these findings, smaller tumors were observed in the livers of syringin-treated mice at the time of sacrifice (Fig. 1L and M). In a subcutaneous Hepa1-6 tumor model in BALB/c nude mice, syringin also markedly suppressed tumor growth (Fig. S1N−S1P), suggesting that syringin-mediated inhibition of tumor growth did not depend on T cells. Collectively,

4 + IL-13 (20 ng/mL each), syringin reduced *Arg1*, *Mrc1*, and *Il10* mRNA levels. Comparisons were made against the IL-4 + IL-13 group. (J) Schematic of the orthotopic HCC model and dosing schedule. Syringin (40 mg/kg) was administered intraperitoneally as indicated ($n = 5$ mice per group). (K) *In vivo* imaging demonstrated that syringin suppressed tumor growth over time. (L) Representative images of mouse livers collected at necropsy. Scale bar: 1 cm. (M) H&E staining of tumor sections. Scale bars: top, 0.5 cm; bottom, 200 μm. Data are presented as mean ± SD, $*P < 0.05$, $**P < 0.01$, $***P < 0.001$.

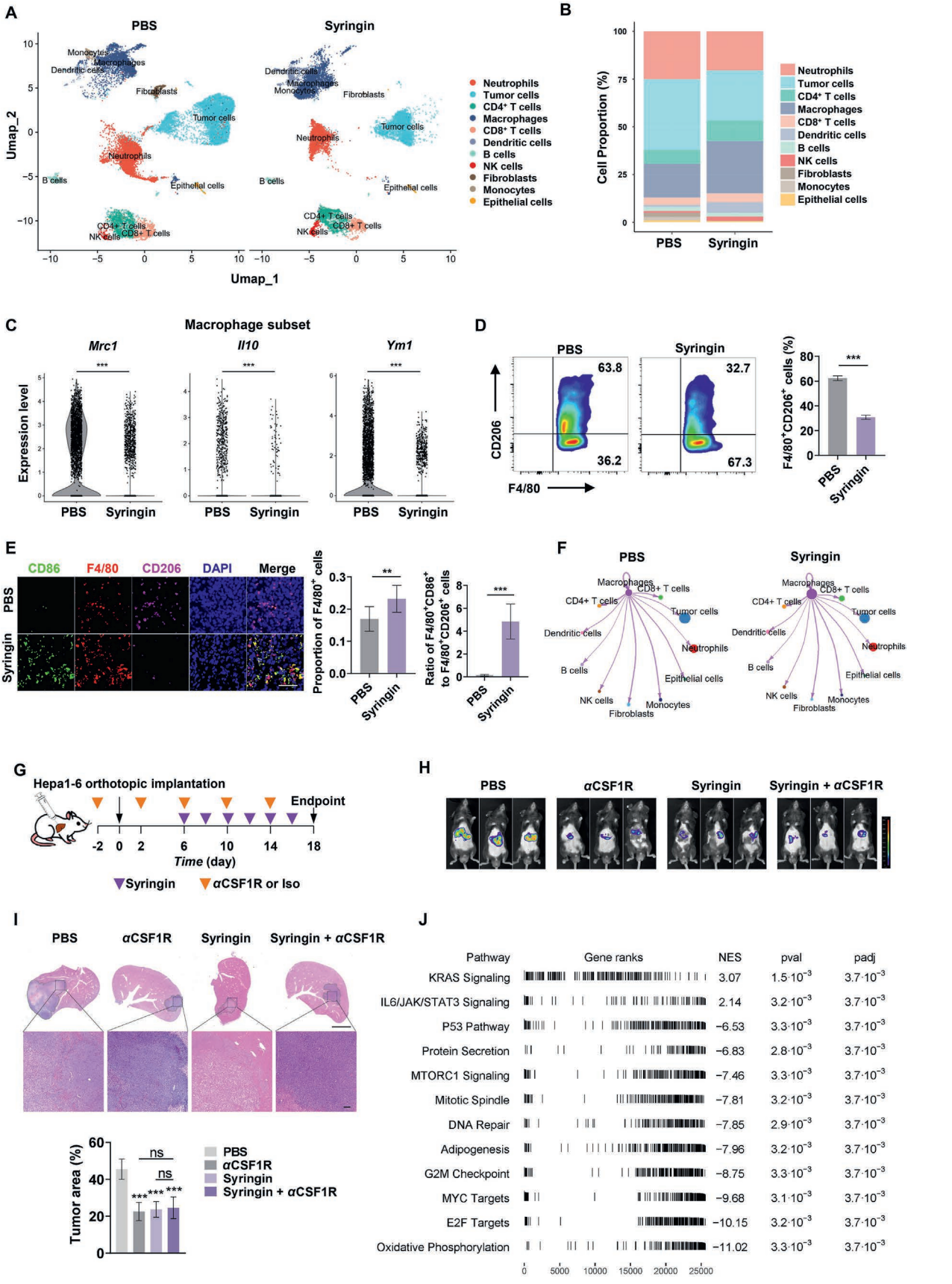

Figure 2 Syringin inhibits HCC by modulating TAM polarization. (A, B) Single-cell RNA sequencing (scRNA-seq) analysis of orthotopic HCC tumors. (A) The uniform manifold approximation and projection (UMAP) plot showing clustering of distinct cell populations. (B)

these results suggest that syringin's antitumor effects are likely associated with macrophage polarization rather than directly targeting tumor cells or relying on T-cell cytotoxicity. In addition, H&E staining of major organs revealed no structural abnormalities, indicating that syringin treatment did not cause significant toxicity (Fig. S1Q).

3.2. Syringin reshapes TME remodeling to suppress HCC progression by blocking TAM polarization

The therapeutic potential of syringin in reshaping the immunosuppressive TME was further investigated. ScRNA-seq was performed to analyze the impact of syringin on the TME in the Hepa1-6 orthotopic HCC model. As expected, syringin reduced the tumor cell proportion and enhanced immune cell infiltration, with significant shifts in macrophage distribution observed in the UMAP plot (Fig. 2A and B, Supporting Information Fig. S2A). Macrophages were subclustered using AddModuleScore with M1/M2 gene signatures (Table S3) to define three subsets: M1-like, M2-like, and naïve (Fig. S2B and S2C). Compared with the PBS group, syringin significantly decreased M2-like and increased M1-like macrophage proportions. Concordantly, the fraction of cells expressing M2-associated genes (*Mrc1*, *Il10*, *Ym1*) was reduced (Fig. 2C). In agreement with scRNA-seq, which indicated a higher macrophage abundance (Fig. 2B), flow cytometry confirmed increased overall macrophage infiltration, with the rise in F4/80$^+$CD86$^+$ (M1) cells surpassing the decline in F4/80$^+$CD206$^+$ (M2) cells (Fig. 2D, Fig. S2D and S2E). Consistently, multiplex immunostaining (F4/80, CD86, CD206) of tumor sections showed an increased fraction of F4/80$^+$ cells in syringin-treated tumors, with a dramatic rise in F4/80$^+$CD86$^+$ and a moderate reduction in F4/80$^+$CD206$^+$ subsets (Fig. 2E). Cell−cell communication analysis also predicted macrophages as the primary source of altered ligands among all subpopulations (Fig. 2F). These findings provide compelling evidence that syringin suppresses the M2 polarization of TAMs in HCC.

Depletion of TAMs *via* CSF1R blockade significantly impaired tumor growth[26]. To further investigate the role of TAMs in syringin's antitumor activity, we combined syringin treatment with αCSF1R-mediated TAM depletion in the orthotopic HCC model (Fig. 2G). Notably, αCSF1R alone significantly reduced tumor growth, whereas syringin reduced growth under isotype control but showed no additional effect in the presence of αCSF1R (Fig. 2H and I). Similar results were observed in a model of SB transposon-driven hepatocarcinogenesis (Fig. S2F and S2G). These findings indicate that syringin's antitumor effect is largely dependent on macrophage modulation.

Based on scRNA-seq data, Gene Set Enrichment Analysis (GSEA) was conducted to assess the impact of syringin on signaling pathways in the macrophage subset. The analysis revealed several downregulated pathways, with MYC targets, E2F targets, and oxidative phosphorylation (OXPHOS) exhibiting the most pronounced alterations (Fig. 2J and S2H). Several genes in the OXPHOS pathway, downregulated following syringin treatment, were part of the MYC target gene set, further supporting that syringin blocked MYC to reshape the TME.

3.3. Syringin regulates macrophage M2 polarization via MYC

MYC functions as a central regulator of intracellular metabolism, coordinating pathways such as OXPHOS to balance cellular energy demands and biosynthetic processes[27,28]. To further explore syringin's mechanism of action, we examined its effect on MYC expression. In IL-4-stimulated BMDMs, MYC levels were significantly upregulated (Fig. 3A), consistent with its established role as a functional indicator of M2 polarization[29]. Syringin treatment led to a dose-dependent decrease in MYC expression (Fig. 3A). Additionally, downstream targets of MYC, including *Dusp2*, *Pa2g4*, *Cox8a*, and *Idh3b*, were downregulated following syringin treatment (Fig. 3B). Syringin also suppressed the expression of these MYC target genes in IL-4 + IL-13-stimulated THP-1 macrophages (Supporting Information Fig. S3A), demonstrating its consistent inhibitory effect on MYC-regulated pathways in M2 polarization.

MYC-driven metabolic reprogramming underpins M2 polarization[27,28]. Knockdown of *Myc* in BMDMs markedly reduced *Arg1*, *Mrc1*, and *Il10* expression, while reintroduction of shRNA-resistant rMYC restored the expression of these M2 markers, highlighting the critical role of MYC in regulating M2 polarization (Fig. S3B and S3C). In syringin-treated BMDMs, MYC overexpression significantly reversed syringin's effects on *Arg1* and *Mrc1*, as well as IL-10 (Fig. 3C−E). Conversely, *Myc* knockdown mimicked the effect of syringin on these M2 markers, while restoration of MYC expression reproduced syringin's regulatory effects (Fig. 3F−H). The expression of *Dusp2*, *Pa2g4*, *Cox8a*, and *Idh3b* was consistent with MYC protein levels in syringin-treated BMDMs (Fig. S3D).

Subsequently, we utilized macrophage-specific *Myc* knockout mice (*Lyz2*$^+$*Myc*$^{f/f}$) to validate the role of MYC in syringin-mediated inhibition of M2 polarization and HCC progression. *Myc*$^{f/f}$ mice served as controls. F4/80$^+$CD11b$^+$ macrophages were isolated from tumors to confirm the efficiency of *Myc* knockout in *Lyz2*$^+$*Myc*$^{f/f}$ mice (Fig. S3E). Under IL-4-induced M2 polarization, syringin significantly decreased IL-10 secretion in BMDMs from *Myc*$^{f/f}$ mice, but not in those from *Lyz2*$^+$*Myc*$^{f/f}$ mice (Fig. 3I). CD206 expression in BMDMs also yielded comparable results (Fig. 3J). *In vivo*, *Lyz2*$^+$*Myc*$^{f/f}$ mice exhibited reduced orthotopic tumor growth compared with *Myc*$^{f/f}$ controls (Fig. 3K and L). Syringin suppressed tumor growth in *Myc*$^{f/f}$ mice, but had minimal effect in *Lyz2*$^+$*Myc*$^{f/f}$ mice, likely because syringin did not alter the proportion of F4/80$^+$CD206$^+$ macrophages in *Lyz2*$^+$*Myc*$^{f/f}$ mice (Fig. 3M). CD86 expression was not

Distribution of cell populations within the tumor microenvironment (TME). Tumors from 3 mice per group were pooled to generate each library. (C) Expression of *Mrc1*, *Il10*, and *Ym1* in the macrophage subset. (D) Flow cytometry analysis showing that syringin decreased the proportion of F4/80$^+$CD206$^+$ macrophages in tumors ($n = 3$). (E) Multiplex immunostaining for F4/80, CD86, and CD206 in tumor sections also revealed altered abundance and composition of tumor-associated macrophages (TAMs). Quantitative image analysis was performed using 5 mice per group. Scale bar: 100 μm. (F) CellChat analysis illustrating the impact of syringin on cell-cell communication networks within the TME. (G) Schematic of the experimental design for macrophage depletion using anti-CSF1R antibody (αCSF1R) ($n = 6$). (H, I) *In vivo* imaging (H) and H&E staining (I) of tumors following treatment with syringin (40 mg/kg) and αCSF1R (200 μg/mouse). Scale bars: top, 0.5 cm; bottom, 200 μm. (J) GSEA of scRNA-seq data identifying pathways affected by syringin in macrophages. Data are presented as mean ± SD, $^{**}P < 0.01$, $^{***}P < 0.001$.

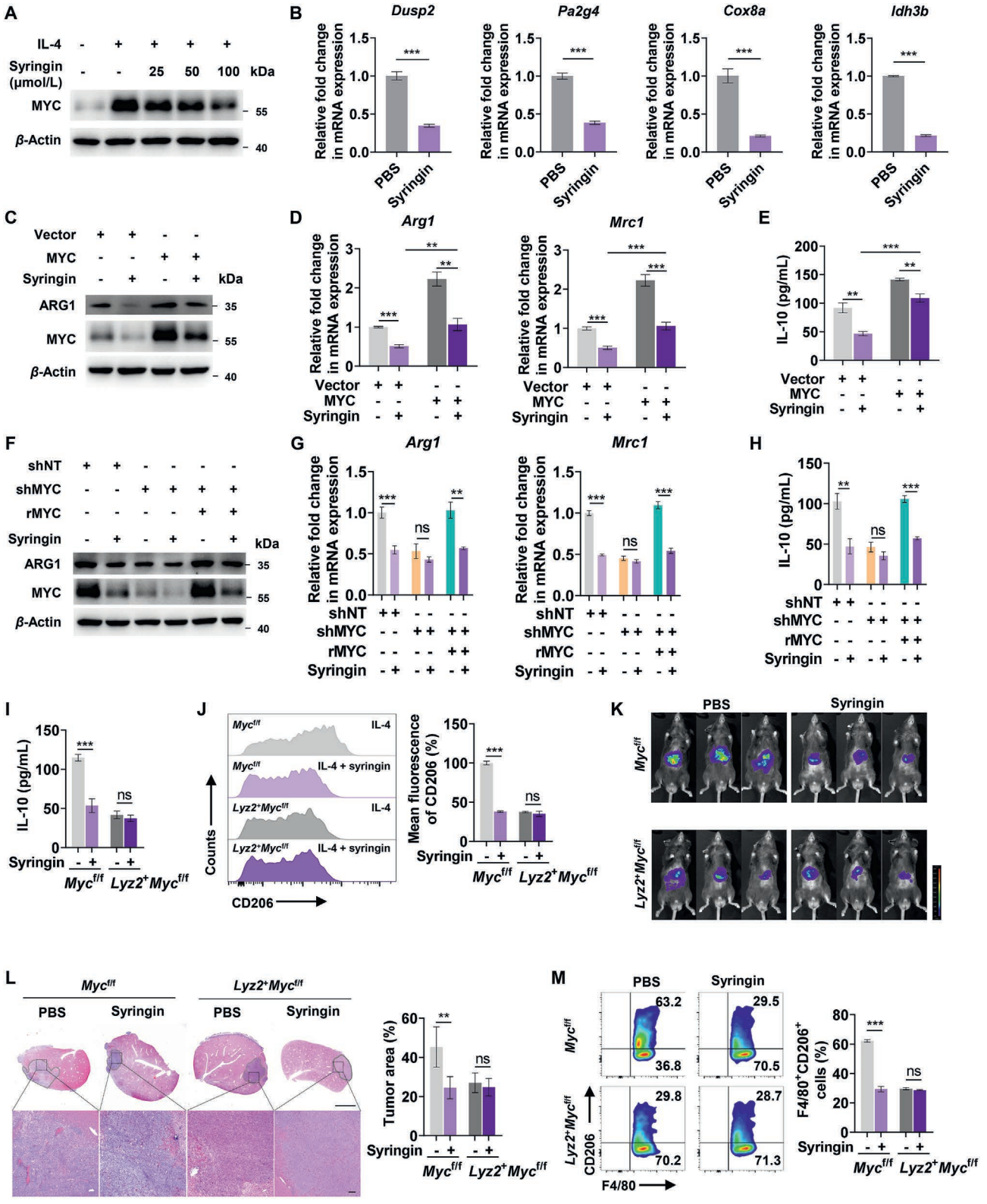

Figure 3 Syringin inhibits macrophage M2 polarization in a MYC-dependent manner. (A) Syringin reduced MYC protein levels during M2 polarization. (B) Syringin modulated the expression of MYC downstream genes (*Dusp2*, *Pa2g4*, *Cox8a*, and *Idh3b*) in IL-4-treated BMDMs. (C–E) Overexpression of MYC (C) attenuated the inhibitory effects of syringin on *Arg1* and *Mrc1* expression (D) and on IL-10 secretion (E) in IL-4-polarized BMDMs. (F–H) MYC was required for the inhibitory effect of syringin. MYC knockdown (F) abrogated syringin-mediated suppression of *Arg1*, *Mrc1* (G), and IL-10 (H), whereas reconstitution with shRNA-resistant rMYC restored the suppression. (I) IL-10 secretion in supernatants of IL-4-polarized BMDMs isolated from $Myc^{f/f}$ and $Lyz2^{+}Myc^{f/f}$ mice. (J) Syringin reduced CD206 expression in BMDMs from $Myc^{f/f}$ mice but not $Lyz2^{+}Myc^{f/f}$ mice. (K, L) *In vivo* imaging (K) and H&E staining (L) of the tumors in $Myc^{f/f}$ and $Lyz2^{+}Myc^{f/f}$ mice with or

significantly altered by *Myc* knockout in LPS and IFN-γ-stimulated BMDMs, whereas syringin elicited a modest increase in CD86 expression, irrespective of MYC status (Fig. S3F). Moreover, syringin failed to further inhibit HCC progression in $Lyz2^{+}Myc^{f/f}$ mice bearing SB transposon-driven primary liver cancer (Fig. S3G and S3H), consistent with the orthotopic tumor results. These findings provide a MYC-dependent mechanism underlying syringin-mediated tumor suppression and M2 polarization.

3.4. Syringin binds directly to DLAT

MYC protein was reduced by syringin, yet *Myc* mRNA remained unaffected (Fig. 4A). This paradox suggested that syringin regulated MYC post-transcriptionally, potentially by modulating its stability. A CHX chase assay was used to examine MYC protein degradation, showing a rapid reduction within 30 min, indicating rapid turnover (Fig. 4B). Syringin treatment accelerated MYC protein degradation, as evidenced by the CHX chase assay (Fig. 4B).

The binding of small molecules can disrupt protein stability[30]. However, syringin did not affect MYC thermal stability in the cellular thermal shift assay (CETSA) (Fig. 4C), implying an indirect binding mechanism between syringin and MYC. MYC degradation primarily occurs through the ubiquitin-proteasome pathway, where its stability depends on the extent of ubiquitination[31]. Acetylation and SUMOylation of MYC can perturb ubiquitination, thereby modulating its stability. Paired short- and long-exposure immunoblots of MYC immunoprecipitates revealed increased MYC ubiquitination after syringin treatment (Fig. 4D and Supporting Information Fig. S4A). Treatment with MG132 completely abrogated the syringin-induced reduction in MYC, suggesting that syringin regulated MYC stability *via* a ubiquitin-dependent degradation pathway. Under short exposure, increased MYC ubiquitination with syringin was apparent in the presence of MG132 (Fig. 4D). At long exposure, an increased ubiquitinated MYC fraction with syringin was also observed without MG132, consistent with enhanced proteasomal turnover (Fig. 4D and S4A). In addition, a tandem ubiquitin-binding entity (TUBE) pulldown followed by anti-MYC immunoblotting corroborated the increase in ubiquitinated MYC after syringin treatment (Fig. S4B).

To identify the direct targets of syringin, a clickable azide tag was incorporated into its structure by modifying the synthesis route (Fig. S4C−S4G) [32]. After incubation with IL-4-stimulated BMDMs, the syringin-p underwent a click reaction with DBCO-AF488, allowing assessment of its subcellular localization. These results revealed cellular uptake and predominant cytoplasmic distribution of syringin in M2 macrophages (Fig. 4E). To identify potential targets of syringin, a competitive ABPP assay was performed, in which M2-polarized BMDMs were pre-incubated with syringin to block target protein binding, followed by labeling with the syringin-p to selectively profile syringin-specific target proteins (Fig. 4F). Proteins bound to syringin-p were identified using mass spectrometry, as described previously[33]. DLAT was among the top candidates, and its binding to syringin-p was markedly decreased upon syringin treatment (Fig. 4G and H). Interestingly, DLAT has been implicated in direct interaction with MYC in tumor cells[25]. BLI was employed to characterize the interaction between recombinant DLAT and syringin, revealing a high-affinity direct association (Fig. 4I). The binding was further corroborated by the CETSA, which demonstrated that syringin enhanced the thermal stability of DLAT in M2 macrophages (Fig. 4J).

3.5. Syringin inhibits MYC acetylation and promotes its degradation through DLAT

Previous studies have identified DLAT as a potential regulator of macrophage metabolism[34]. Moreover, recent studies reported that DLAT acts as an acetyltransferase, acetylating the AU RNA binding protein/enoyl-CoA hydratase (AUH) at K109 and MYC at K148, thereby stabilizing MYC[25,35]. However, the association between DLAT and MYC in macrophages has yet to be characterized. In M2-polarized BMDMs, reciprocal co-immunoprecipitation with anti-MYC and anti-DLAT antibodies confirmed the interaction between MYC and DLAT (Fig. 5A). Subsequent analysis showed that syringin significantly decreased MYC acetylation, both in the presence and absence of MG132 (Fig. 5B). Based on the interaction between syringin and DLAT, along with its effect on MYC acetylation, we hypothesized that syringin regulates MYC stability by modulating DLAT activity.

In the presence of acetyl-CoA, DLAT transfers an acetyl group to MYC[25]. In an *in vitro* enzymatic activity assay, syringin significantly inhibited the acetyltransferase activity of DLAT, as evidenced by reduced acetylation of lysine residues on MYC (Fig. 5C). The binding of DLAT to MYC was unaffected by syringin (Supporting Information Fig. S5A). However, syringin almost completely abrogated the interaction between DLAT and acetyl-CoA in the BLI assay (Fig. S5B). These findings suggest that syringin interferes with DLAT binding to acetyl-CoA, thereby inhibiting DLAT-mediated MYC acetylation.

The binding mode of syringin to DLAT was predicted using molecular docking. The results showed that syringin likely interacts with DLAT through hydrogen bonds (I427, R430, I575, and N576) and hydrophobic interactions (I427, R430, L431, and L516) (Fig. 5D and Fig. S5C). To confirm the binding sites, a series of truncated DLAT fragments (full-length: aa 1−642; t1: aa 1−529; t2: aa 1−499; t3: aa 1−411; Fig. S5D) were generated and assessed for their binding affinity to syringin (Fig. 5E and S5E). Compared with full-length DLAT, syringin exhibited a substantially lower binding affinity for all truncated variants. Among them, syringin exhibited comparable binding affinities (K_d values) for t1 and t2, while virtually no binding was observed with t3. These results indicated that the critical residues required for syringin binding are located within the S2 and S4 regions of DLAT. To identify the key residues involved in syringin binding to DLAT, we generated DLAT mutants R430A, N576K, and the double mutant R430A + N576K, as R430 and N576 were predicted to be critical for syringin binding. Binding assays showed decreased affinity of the DLAT R430A or N576K mutants for syringin, with the double mutant exhibiting almost negligible binding (Fig. 5F).

DLAT acetyltransferase activity toward MYC was unchanged for the R430A, N576K, and R430A + N576K mutants relative to the wild type *in vitro*, yet syringin failed to inhibit the DLAT R430A + N576K mutant-mediated MYC acetylation (Fig. 5G).

without syringin ($n = 6$ mice per group). Scale bars: top, 0.5 cm; bottom, 200 μm. (M) Quantification of $F4/80^{+}CD206^{+}$ cells in tumors from different treatment groups ($n = 3$). Data are presented as mean ± SD, $^{**}P < 0.01$, $^{***}P < 0.001$.

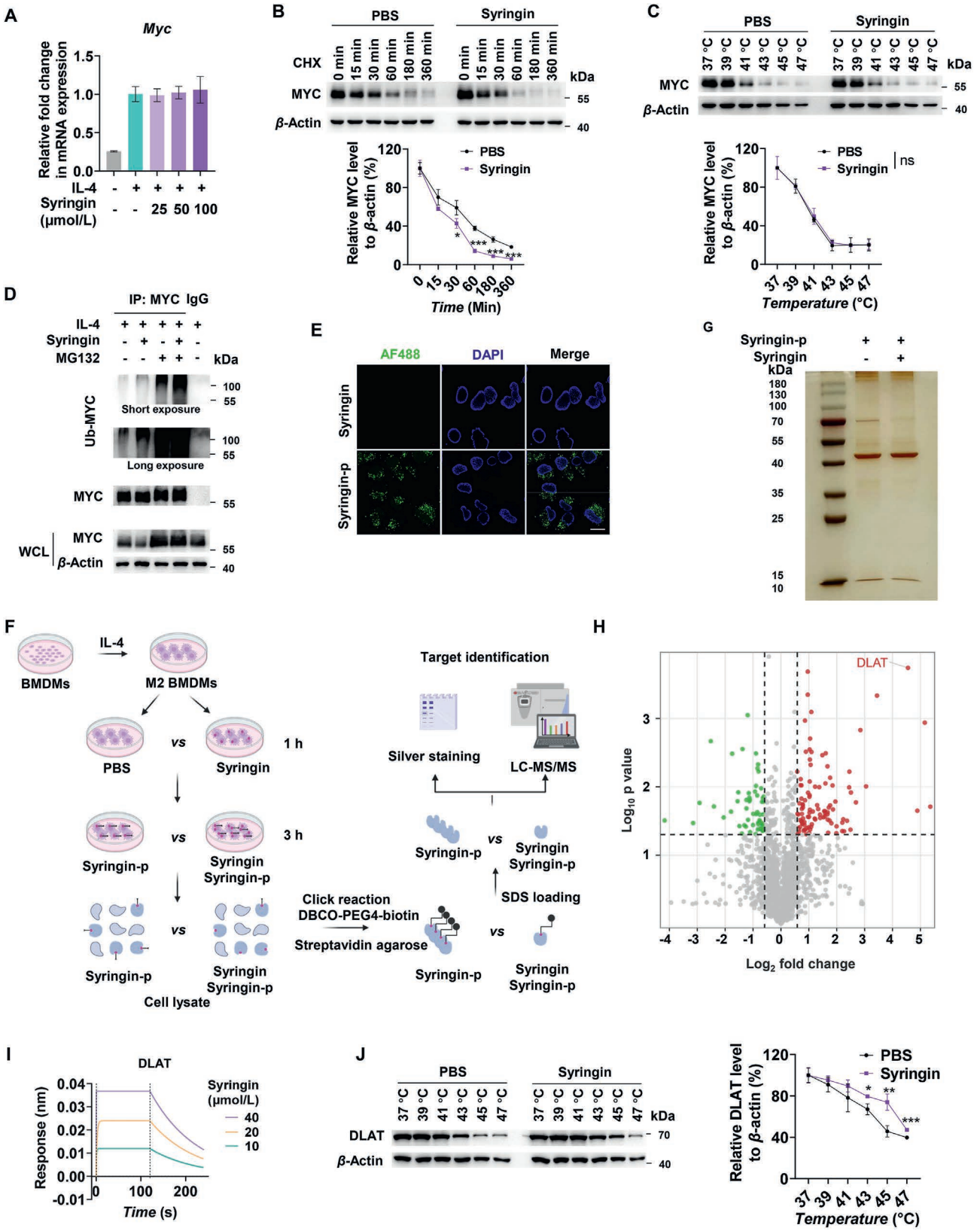

Figure 4 Syringin directly binds to DLAT. (A) Syringin did not alter *Myc* mRNA levels in IL-4-polarized BMDMs. (B) Syringin promoted MYC protein degradation. MYC levels were assessed using a cycloheximide (CHX)-mediated protein turnover assay. (C) Syringin had minimal effect on the thermal stability of MYC. IL-4-polarized BMDMs were treated with syringin (100 μmol/L) for 3 h prior to lysis. (D) Syringin enhanced MYC ubiquitination. Immunoprecipitation was performed using an anti-MYC antibody or IgG. BMDMs were treated with syringin and IL-4 for 22 h, followed by incubation with or without MG132 (20 μmol/L) for 2 h to inhibit ubiquitin-proteasome-mediated degradation. (E)

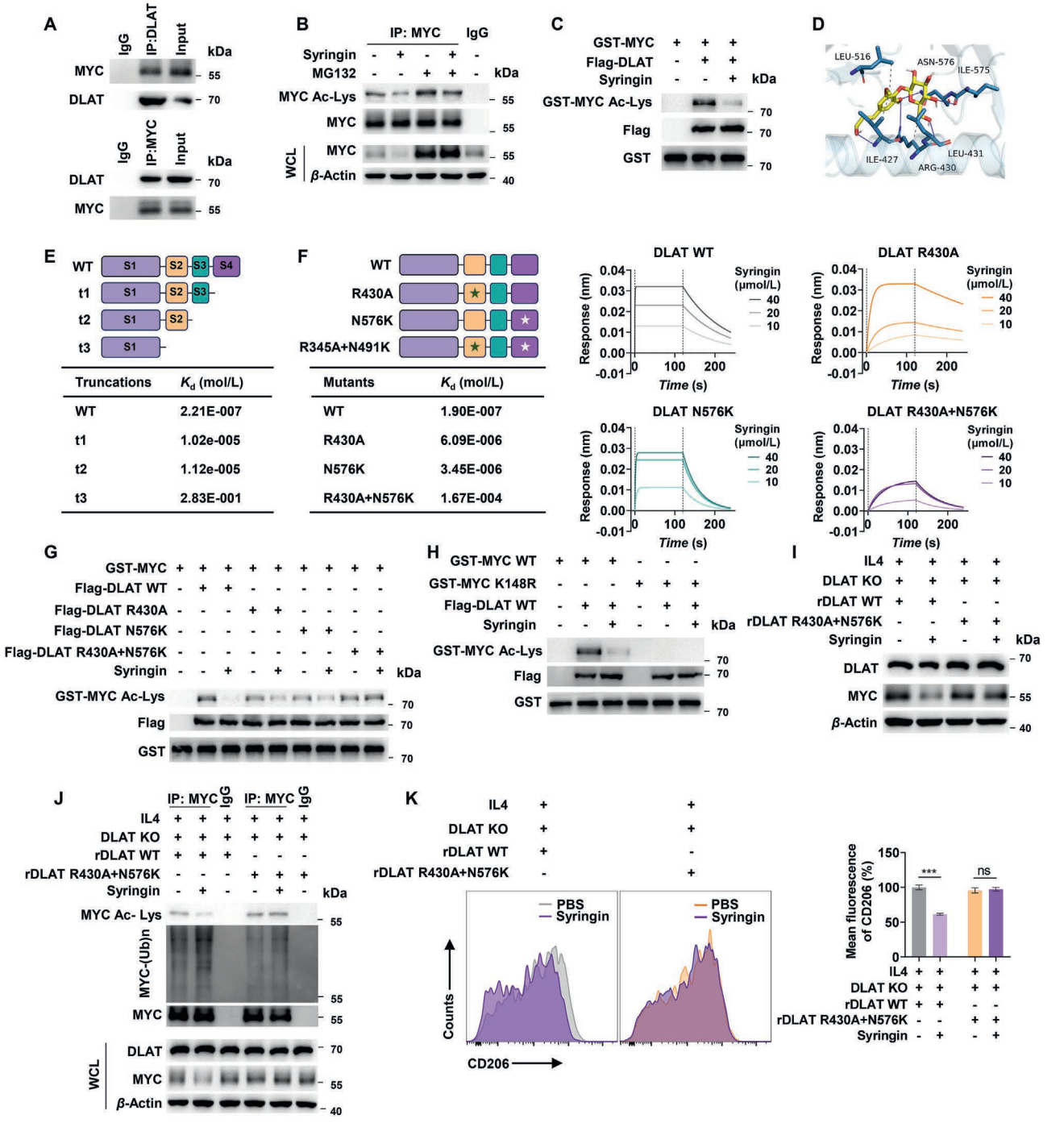

Figure 5 Syringin targets DLAT and inhibits MYC acetylation to suppress M2 polarization. (A) Co-immunoprecipitation analysis showed the interaction between DLAT and MYC in IL-4-polarized BMDMs. (B) Syringin inhibited MYC acetylation in macrophages. (C) *In vitro* assay demonstrated the inhibitory effect of syringin on DLAT-mediated MYC acetylation. (D) Molecular docking simulated the interaction between syringin and DLAT. ILE, I; ARG, R; LEU, L; ASN, N. (E) BLI analysis revealed different binding affinities of syringin for truncated DLAT fragments. (F) BLI analysis confirmed that point mutations in DLAT altered its binding to syringin. (G) DLAT mutations (R430A and/or N576K) weakened syringin's ability to inhibit DLAT-mediated MYC acetylation. Lys, K. (H) The MYC K148R mutation abolished DLAT-mediated MYC acetylation. (I, J) In iBMDMs expressing DLAT R430A + N576K, syringin failed to alter MYC protein levels, acetylation, or ubiquitination. (K) In IL-4-treated iBMDMs, syringin reduced CD206 expression in DLAT WT cells but not in DLAT R430A + N576K cells. Data are presented as mean ± SD, $^{***}P < 0.001$.

Syringin-p was internalized into cells. Scale bar: 10 μm. (F) Workflow for profiling syringin target proteins. (G, H) Silver staining (G) and LC−MS/MS analysis (H) of proteins interacting with syringin. (I) Biolayer interferometry (BLI) analysis demonstrated direct interaction between syringin and recombinant DLAT. (J) Cellular thermal shift assay (CETSA) confirmed an interaction between syringin and DLAT in IL-4-polarized BMDMs. Data are presented as mean ± SD, $^{*}P < 0.05$, $^{**}P < 0.01$, $^{***}P < 0.001$.

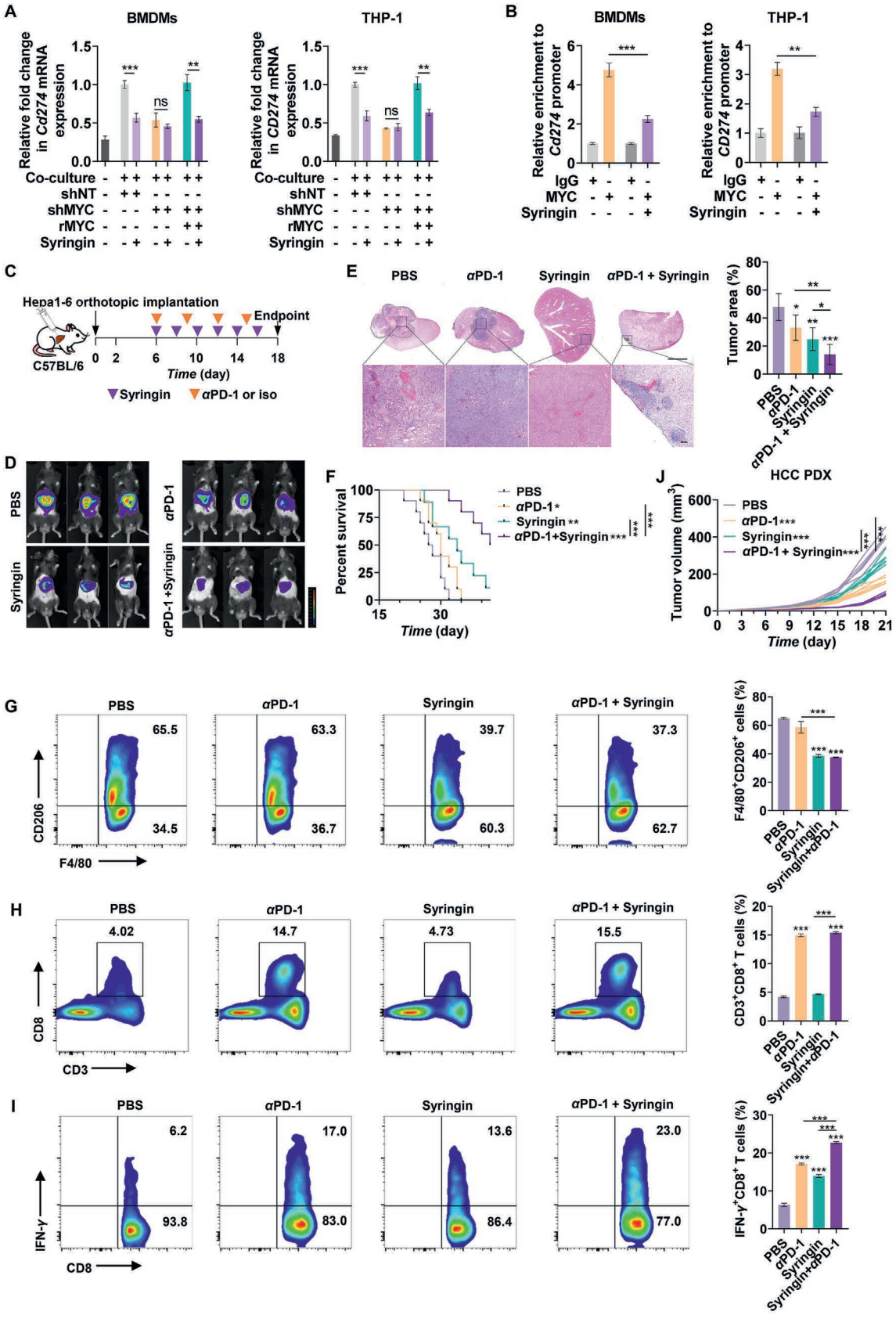

Figure 6 Synergistic effect of syringin and anti-PD-1 immunotherapy. (A) MYC knockdown downregulated *Cd274* mRNA in BMDMs co-cultured with Hepa1-6 cells and *CD274* mRNA in THP-1 cells co-cultured with Huh7 cells. (B) Syringin reduced MYC occupancy at the *Cd274*/*CD274* promoters in BMDMs and THP-1 cells. (C) Schematic illustration of the experimental design. (D) *In vivo* bioluminescence

Consistently, the MYC K148R mutation completely abolished MYC acetylation by DLAT, in line with previous reports (Fig. 5H)[25]. These findings highlighted the critical roles of residues R430 and N576 for DLAT binding and inhibition by syringin.

Immortal bone marrow-derived macrophages (iBMDMs) recapitulate the metabolic features and activation states of primary BMDMs, while being more amenable to stable genetic transformation[36]. Under IL-4 stimulation, DLAT knockdown in iBMDMs decreased MYC and CD206 expression, rendering syringin largely ineffective (Fig. S5F and S5G). To validate DLAT as the target of syringin, we generated DLAT-knockout iBMDMs and reintroduced the binding-defective DLAT R430A + N576K mutant (Fig. S5H). The DLAT R430A + N576K mutant did not compromise DLAT-mediated acetylation of MYC (Fig. 5I and J). In wild-type iBMDMs under IL-4 stimulation, syringin reduced MYC expression and altered its acetylation and ubiquitination (Fig. 5I and J). By contrast, these effects were absent in iBMDMs expressing DLAT R430A + N576K. Consistently, syringin reduced CD206 expression in IL-4-treated wild-type iBMDMs but not in cells expressing DLAT R430A + N576K (Fig. 5K). Collectively, these findings suggest that syringin modulates M2 polarization *via* DLAT, with residues R430 and N576 serving as critical binding sites.

3.6. Syringin enhances the therapeutic efficacy of PD-1/PD-L1 blockade in HCC

The crosstalk between macrophages and other immune cell subsets contributes to the immunosuppressive TME[37]. For example, macrophages express PD-L1, which has been shown to blunt the therapeutic efficacy of PD-1/PD-L1 blockade[38]. Interestingly, we observed reduced PD-L1 expression on F4/80$^+$ TAMs following syringin treatment (Supporting Information Fig. S6A). MYC overexpression correlates with elevated PD-L1 across cancers[39,40]. Conversely, MYC knockdown or inhibition lowers PD-L1 mRNA and protein levels in tumor cells, at least partly because MYC directly binds the PD-L1 promoter to drive its transcription[39]. MYC knockdown significantly decreased *Cd274* (the gene encoding PD-L1) expression in M2-polarized BMDMs and *CD274* expression in M2-polarized THP-1 cells (Fig. 6A). Syringin reduced *Cd274* expression in MYC-expressing macrophages but not in MYC-knockdown cells, consistent with a MYC-dependent mechanism. ChIP-qPCR confirmed MYC binding at the *Cd274* promoter, and syringin attenuated MYC-driven transcriptional activation of *Cd274* (Fig. 6B). In addition to macrophages, syringin modestly yet reproducibly reduced *Cd*274 mRNA and PD-L1 in Hepa1-6 cells (Fig. S6B and S6C). *In vivo*, syringin also lowered PD-L1 expression within the CD45$^-$ tumor-cell compartment, indicating that its PD-L1-lowering effect extends beyond TAMs (Fig. S6D). In immunocompetent hosts, down-modulation of PD-L1 on both tumor cells and TAMs may jointly contribute to enhanced responses to PD-1/PD-L1 blockade.

We therefore examined whether syringin could potentiate PD-1/PD-L1 blockade (Fig. 6C). Consistent with previous studies[41,42], treatment with αPD-1 delayed tumor growth to a moderate extent (Fig. 6D and E). Combination therapy with syringin and αPD-1 significantly inhibited tumor growth and prolonged survival compared to monotherapy (Fig. 6D−F). Flow cytometry analysis revealed a reduced proportion of F4/80$^+$CD206$^+$ TAMs in mice treated with syringin alone or in combination with αPD-1 (Fig. 6G). Moreover, syringin did not significantly alter CD8$^+$ T cell infiltration, but increased the proportion of IFN-γ$^+$CD8$^+$ T cells (Fig. 6H and I). In contrast, αPD-1 significantly enhanced CD8$^+$ T cell infiltration and increased the proportion of IFN-γ$^+$CD8$^+$ T cells. Combination treatment with syringin and αPD-1 further elevated the proportion of IFN-γ$^+$CD8$^+$ T cells. In an SB transposon-induced liver cancer model as well as a PDX model, the combination of syringin and αPD-1 also demonstrated synergistic efficacy in suppressing tumor growth (Fig. 6J, Fig. S6E and S6F). These data collectively demonstrate that syringin enhances the therapeutic efficacy of PD-1/PD-L1 blockade in HCC.

4. Discussion

Natural products are a rich reservoir of structurally diverse bioactive compounds, many of which exhibit complementary or opposing activities. Phenylethanoid and phenylpropanoid glycosides represent a major class of bioactive constituents in certain traditional Chinese medicines, such as *Acanthopanax* and *Cistanche*. These medicinal plants are recorded in ancient texts for immunomodulatory effects and are recognized for potent bioactivity with minimal toxicity[43,44]. Several studies, including our own, have highlighted that many phenylethanoid and phenylpropanoid glycosides block M1 polarization of macrophages[13,45]. However, syringin demonstrates a distinct mechanism of action in HCC, predominantly inhibiting M2 polarization while promoting M1 polarization. Recent publications have provided valuable insights into the immunomodulatory activity of syringin in autoimmune and metabolic diseases[46-51], yet its relevance to cancer remains poorly characterized. Macrophages exhibit marked context-dependent plasticity, with their functional states dynamically shaped by metabolic stress, cytokine gradients, and intercellular interactions within the tumor microenvironment. These observations warrant an HCC-specific mechanistic delineation of syringin, particularly within the macrophage compartment. Moreover, the direct molecular targets of syringin remain undefined. ABPP is a chemical proteomics approach for identifying direct intracellular targets. In this study, we designed and synthesized a syringin-derived azide probe (syringin-p) to capture and identify the direct binding targets of syringin in macrophages using a competitive ABPP assay[52-54]. Target enrichment and biological validation experiments confirmed a specific interaction between syringin and DLAT, providing direct biochemical evidence of its mechanism of action. Further docking and binding assays revealed hydrogen-bonding interactions between syringin and DLAT, in which both the hydroxyl groups on the sugar moiety and the methoxy oxygen on the aromatic ring of syringin contact key residues of DLAT. These findings underscore that both the glycone and the aglycone are critical determinants of the overall bioactivity of syringin.

imaging showed orthotopic tumor growth. (E) H&E staining of liver sections and quantification of tumor size ($n = 6$ mice per group). Scale bars: top, 0.5 cm; bottom, 200 μm. (F) Survival curves of mice in different treatment groups ($n = 9-10$ mice per group). (G−I) Flow cytometric analysis of F4/80$^+$CD206$^+$ macrophages (G), CD8$^+$ T cells (H), and IFN-γ$^+$CD8$^+$ T cells (I) in tumors ($n = 3$). Syringin (40 mg/kg) and αPD-1 (250 μg per mouse) were administered intraperitoneally as indicated. (J) Effects of syringin and αPD-1 in a PDX model ($n = 6$). Data are presented as mean ± SD, $^*P < 0.05$, $^{**}P < 0.01$, $^{***}P < 0.001$.

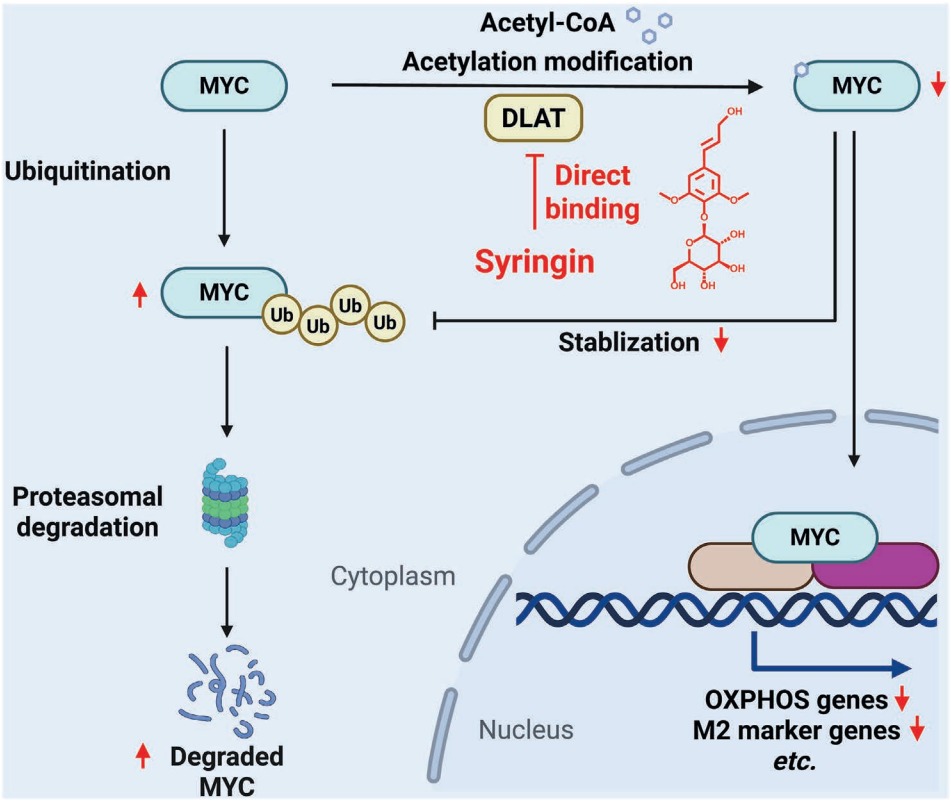

Figure 7 Schematic model of syringin disrupting the DLAT−MYC axis to dampen TAM polarization. Created in BioRender. Xiao, L. (2026) https://BioRender.com/t0v6usr.

TAMs predominantly exhibit an M2-like phenotype and engage in complex, bidirectional interactions with tumor cells and other immune components within the TME, thereby facilitating tumor growth, metastasis, and therapy resistance. However, TAMs also exhibit plasticity, and alterations in their polarization can dynamically shift their roles in HCC. Consequently, merely quantifying TAMs within tumors is insufficient to fully assess their impact on HCC progression. For example, increased densities of CD206-positive TAMs correlate with poor overall and disease-free survival, whereas a higher presence of CD169-positive TAMs is associated with better prognostic outcomes[9]. Modulating macrophage polarization is thus a promising therapeutic strategy in HCC. Several studies provide compelling evidence for this approach. Bufalin, for instance, promotes p65−p50 heterodimer formation while limiting p50 homodimers, thereby activating NF-κB signaling and driving M1 polarization in macrophages[55]. Ligustilide inhibits Yes-associated protein (YAP) expression and nuclear translocation, thereby facilitating a shift toward the M1 phenotype and inhibiting HCC progression[56]. Regorafenib, a clinically approved treatment for HCC, disrupts the p38 mitogen-activated protein kinase (MAPK) pathway, downregulating downstream targets such as *Creb1* and *Klf4*, ultimately inhibiting M2 polarization and enhancing antitumor immunity[57]. Although these compounds are still in early stages of research or have not yet been translated into clinical use as TAM-modulating agents, they highlight the therapeutic potential of macrophage polarization regulation as a promising strategy for HCC management.

Macrophage polarization involves cellular metabolic reprogramming[58]. M2 macrophages are characterized by enhanced OXPHOS, with concurrent increases in glutamine metabolism and fatty acid oxidation. Genes governing metabolic reprogramming orchestrate macrophage polarization. For instance, oncoprotein-induced transcript 3 (OIT3), which is required for hepatic triacylglycerol transport, promotes M2 polarization in macrophages and enhances the metastatic potential of tumor cells when overexpressed[59].

The MYC protein, a master transcription factor regulating cellular metabolism, is required for driving a broad set of targets including *Arg1*, *Il10*, *Ym1*, *Mrc1*, and *Cd274*[27,60]. MYC is significantly elevated in M2-polarized macrophages[27,28]. It promotes M2 polarization through multiple mechanisms. RNA sequencing analysis has shown that in MYC-deficient cells, the OXPHOS gene signature is significantly suppressed, with mitochondrial complexes I to V notably downregulated[61]. MYC knockdown or knockout results in reduced basal oxygen consumption, ATP production, and maximal mitochondrial oxygen consumption[62]. Regulation of OXPHOS by MYC likely constitutes a key mechanism underlying M2 polarization. Additionally, MYC directly promotes CD206 expression in TAMs[63]. Upon IL-4 stimulation, elevated MYC protein facilitates the induction of signal transducer and activator of transcription 6 (STAT6) and peroxisome proliferator−activated receptor gamma (PPARγ), activating a broad range of M2-related polarization markers[27]. In our study, reducing MYC was sufficient to restrain M2-associated features (*e.g.*, Fig. 3I and J, Fig. S3C). Collectively, these features establish MYC as a key determinant of the M2-polarized TAM phenotype. It is also noteworthy that MYC is low or nearly undetectable in resting or M1 macrophages, and pro-inflammatory stimulation (*e.g.*, LPS or IFN-γ) further

suppresses its expression. In our experiments, CD86 expression was not significantly altered by MYC ablation, whereas syringin elicited a modest increase irrespective of MYC status (Fig. S3F). These observations indicate that canonical M1 polarization proceeds largely independently of MYC, whereas M2 polarization depends on MYC activity. In line with this notion, prior work reported that iNOS induction is unaffected by MYC deletion. Moreover, syringin failed to confer additional antitumor efficacy in macrophage-specific MYC-deficient mice (Fig. 3K and L, Fig. S3G and S3H), indicating that its immunomodulatory activity is primarily mediated through suppression of MYC-driven M2 polarization.

The functions of MYC are tightly regulated within cells at multiple levels, including transcription, mRNA stability, protein activity, and degradation. A range of MYC-targeting inhibitors is under development[64]. One approach involves suppressing MYC biosynthesis; for instance, inhibitors of the phosphatidylinositol-3 kinase/protein kinase B/mammalian target of rapamycin (PI3K/AKT/mTOR) pathway suppress MYC protein levels by limiting cap-dependent translation[65]. Another strategy targets MYC activity by disrupting the MYC-MAX (MYC-associated factor X) complex or blocking its DNA binding[64]. However, these inhibitors have yet to achieve significant clinical success. An alternative approach involves modulating MYC stability *via* protein degradation pathways. MYC is primarily degraded through the ubiquitin−proteasome system, with its turnover regulated by phosphorylation, acetylation, and ubiquitination[66]. For example, F-box and WD repeat domain-containing 7 (FBW7) deficiency in TAMs results in elevated MYC levels, promoting M2 polarization and tumor progression[29]. Targeting MYC stability offers a feasible therapeutic approach, overcoming challenges posed by its intrinsically disordered structure. In this study, syringin was identified as a small molecule that interacts with DLAT to regulate MYC levels, thereby impacting M2 polarization.

Although MYC is essential for tumor cells and was reduced by syringin, direct inhibition of HCC cell proliferation was modest and evident only at high concentrations (Fig. S1E−S1M). Syringin reduced MYC across the tested cell types, but to a lesser extent than shRNA-mediated knockdown (Supporting Information Fig. S7A). In these HCC cell lines, shMYC suppressed proliferation to a greater extent than syringin (Fig. S7B). These data imply that HCC cells may require greater MYC suppression to impair growth, possibly due to compensatory networks, whereas macrophage reprogramming is more sensitive to modest MYC reductions.

The state of TAMs also influences the responses of HCC cells to immunotherapy[67]. Enhancing M2 polarization leads to T cell exhaustion, impairing the efficacy of ICBs in HCC treatment[68]. Conversely, inhibiting M2 and promoting M1 polarization improves sensitivity to ICBs[9]. In this study, we found that MYC upregulation in M2-polarized macrophages directly promotes PD-L1 transcription by binding to its promoter, suggesting a potential mechanism by which TAMs contribute to immunosuppression in HCC. Syringin inhibited M2 polarization, reduced PD-L1 expression on macrophages, and increased IFN-γ production in $CD8^+$ T cells. Combination therapy with syringin and αPD-1 further increased the proportion of IFN-γ^+CD8^+ T cells, suppressed tumor growth, and prolonged survival in tumor-bearing mice.

Notably, syringin did not affect HCC growth in either macrophage-depleted or macrophage-specific MYC knockout mice, indicating a macrophage-centric, MYC-dependent mechanism (Figs. 2G−I, S2F and S2G, 3K−M, and S3G−S3H). In contrast, antitumor efficacy was maintained in BALB/c nude mice lacking functional T cells, supporting $CD8^+$ T cell-independent activity under monotherapy (Fig. S1N−S1P). Syringin also reduced PD-L1 on macrophages and tumor cells, consistent with diminished MYC-dependent promoter activity (Fig. 6A and B, Fig. S6A−S6D), thereby augmenting PD-1/PD-L1 blockade in a largely $CD8^+$ T cell-dependent manner. These observations align with prior work showing that M2-polarized macrophages promote tumor growth directly through the release of cytokines such as IL-10, C-C motif ligand 18 (CCL18), and C−C motif ligand 20 (CCL20), and indirectly by suppressing cytotoxic immune populations including $CD8^+$ T cells[69-71]. Collectively, syringin acts through macrophage MYC to provide $CD8^+$ T cell-independent efficacy as monotherapy and to enhance the efficacy of PD-1/PD-L1 blockade in a $CD8^+$ T cell-dependent manner.

5. Conclusions

In summary, this study identifies syringin, a natural phenylpropanoid glycoside, as a macrophage-targeting compound that reshapes the tumor immune microenvironment in HCC. By directly binding to DLAT, syringin suppresses MYC acetylation and promotes its degradation through the ubiquitin-proteasome pathway, thereby downregulating MYC and inhibiting TAM M2 polarization (Fig. 7). These effects collectively alleviate immunosuppression and restrain tumor growth. Moreover, syringin augments the efficacy of PD-1/PD-L1 blockade, providing a mechanistic basis for its use as a potential macrophage-directed adjunct in HCC therapy.

Acknowledgments

This work was supported by the Natural Science Foundation of Guangdong Province (2025A1515012020), and the National Natural Science Foundation of China (81903914). The graphical abstract was created in BioRender. Xiao, L. (2026) https://BioRender.com/efv04ll.

Author contributions

Lingyun Xiao: Conceptualization, Methodology, Investigation, Data curation, Writing − original draft, Funding acquisition. Jiawei Lv: Methodology, Investigation, Data curation, Writing − original draft. Yuan Lu: Methodology, Investigation, Data curation, Writing − original draft. Zun Li: Methodology, Investigation, Data curation. Liang-Mei Yang: Methodology, Investigation. Zheng Li: Methodology, Investigation. Shu Liang: Methodology, Investigation, Writing − review & editing. Ke-Bin Huang: Writing − review & editing, Supervision. Xiongjun Wang: Conceptualization, Methodology, Writing − review & editing, Supervision, Project administration.

Conflicts of interest

The authors declare no conflicts of interest.

Appendix A. Supporting information

Supporting information to this article can be found online at https://doi.org/10.1016/j.apsb.2026.03.036.

References

1. Llovet JM, Castet F, Heikenwalder M, Maini MK, Mazzaferro V, Pinato DJ, et al. Immunotherapies for hepatocellular carcinoma. *Nat Rev Clin Oncol* 2022;**19**:151−72.
2. Ni X, Li D, Dai S, Pan H, Sun H, Ao J, et al. Development and evaluation of nomograms to predict the cancer-specific mortality and overall mortality of patients with hepatocellular carcinoma. *BioMed Res Int* 2021;**2021**:1658403.
3. Pinter M, Jain RK, Duda DG. The current landscape of immune checkpoint blockade in hepatocellular carcinoma: a review. *JAMA Oncol* 2021;**7**:113−23.
4. Zanuso V, Pirozzi A, Balsano R, Pressiani T, Rimassa L. Safety and efficacy of atezolizumab and bevacizumab combination as a first line treatment of advanced hepatocellular carcinoma. *J Hepatocell Carcinoma* 2023:1689−708.
5. Xu H, Qin X, Guo Y, Zhao S, Feng X, Zhang R, et al. Radiation-based immunogenic vaccine combined with a macrophage "checkpoint inhibitor" for boosting innate and adaptive immunity against metastatic colon cancers. *Acta Pharm Sin B* 2024;**14**:2247−62.
6. Li AQ, Huang F, Talaiti S, Yang X, Bi H, Fang JH. Understanding the complexity of tumor-associated macrophages: druggable and therapeutic insights. *Acta Pharm Sin B* 2025;**15**:4456−75.
7. Murray PJ. Macrophage polarization. *Annu Rev Physiol* 2017;**79**:541−66.
8. Zheng H, Peng X, Yang S, Li X, Huang M, Wei S, et al. Targeting tumor-associated macrophages in hepatocellular carcinoma: biology, strategy, and immunotherapy. *Cell Death Discov* 2023;**9**:65.
9. Li D, Zhang T, Guo Y, Bi C, Liu M, Wang G. Biological impact and therapeutic implication of tumor-associated macrophages in hepatocellular carcinoma. *Cell Death Dis* 2024;**15**:498.
10. Sehgal A, Irvine KM, Hume DA. Functions of macrophage colony-stimulating factor (CSF1) in development, homeostasis, and tissue repair. *Semin Immunol* 2021;**54**:101509.
11. Li X, Yao W, Yuan Y, Chen P, Li B, Li J, et al. Targeting of tumour-infiltrating macrophages *via* CCL2/CCR2 signalling as a therapeutic strategy against hepatocellular carcinoma. *Gut* 2017;**66**:157−67.
12. Han S, Bao X, Zou Y, Wang L, Li Y, Yang L, et al. D-Lactate modulates M2 tumor-associated macrophages and remodels immunosuppressive tumor microenvironment for hepatocellular carcinoma. *Sci Adv* 2023;**9**:eadg2697.
13. Xiao L, Yao J, Miao Y, Ou B, Wang J, Huang Y, et al. Tubuloside B, isolated from Cistanche tubulosa, a promising agent against M1 macrophage activation *via* synergistically targeting Mob1 and ERK1/2. *Biomed Pharmacother* 2022;**153**:113414.
14. Deng Y, Ostermann E, Brune W. A cytomegalovirus inflammasome inhibitor reduces proinflammatory cytokine release and pyroptosis. *Nat Commun* 2024;**15**:786.
15. Zhan M, Ding Y, Huang S, Liu Y, Xiao J, Yu H, et al. Lysyl oxidase-like 3 restrains mitochondrial ferroptosis to promote liver cancer chemoresistance by stabilizing dihydroorotate dehydrogenase. *Nat Commun* 2023;**14**:3123.
16. Li K, Sun L, Wang Y, Cen Y, Zhao J, Liao Q, et al. Single-cell characterization of macrophages in uveal melanoma uncovers transcriptionally heterogeneous subsets conferring poor prognosis and aggressive behavior. *Exp Mol Med* 2023;**55**:2433−44.
17. Matsuda T, Kono T, Taki Y, Sakuma I, Fujimoto M, Hashimoto N, et al. Deciphering craniopharyngioma subtypes: single-cell analysis of tumor microenvironment and immune networks. *iScience* 2024;**27**:111068.
18. Zhu W, Chu H, Zhang Y, Luo T, Yu H, Zhu H, et al. Fructose-1,6-bisphosphatase 1 dephosphorylates IκBα and suppresses colorectal tumorigenesis. *Cell Res* 2023;**33**:245−57.
19. Wang Z, Di Y, Wen X, Liu Y, Ye L, Zhang X, et al. NIT2 dampens BRD1 phase separation and restrains oxidative phosphorylation to enhance chemosensitivity in gastric cancer. *Sci Transl Med* 2024;**16**:eado8333.
20. Sodir NM, Kortlever RM, Barthet VJ, Campos T, Pellegrinet L, Kupczak S, et al. MYC instructs and maintains pancreatic adenocarcinoma phenotype. *Cancer Discov* 2020;**10**:588−607.
21. Huang C, Wang L, Zhuo C, Chen W, Fan H, Hong Y, et al. ID3 enhances PD-L1 expression by restructuring MYC to promote colorectal cancer immune evasion. *Proc Natl Acad Sci U S A* 2025;**122**:e2423490122.
22. Nguyen TV, Li J, Lu C-C, Mamrosh JL, Lu G, Cathers BE, et al. p97/VCP promotes degradation of CRBN substrate glutamine synthetase and neosubstrates. *Proc Natl Acad Sci U S A* 2017;**114**:3565−71.
23. Tey PY, Dufner A, Knobeloch K-P, Pruneda JN, Clague MJ, Urbé S. Rapid turnover of CTLA4 is associated with a complex architecture of reversible ubiquitylation. *J Cell Biol* 2024;**224**:e202312141.
24. Chen CH, Chen IC, Hsu CL, Lu TP, Wang MY, Tsai LW, et al. Characterization of the tumor immune microenvironment in pregnancy-associated breast cancer through multiplex immunohistochemistry and transcriptome analyses. *Breast Cancer Res* 2025;**27**:154.
25. Wang J, Yang Y, Shao F, Meng Y, Guo D, He J, et al. Acetate reprogrammes tumour metabolism and promotes PD-L1 expression and immune evasion by upregulating c-Myc. *Nat Metab* 2024;**6**:914−32.
26. O'Brien SA, Orf J, Skrzypczynska KM, Tan H, Kim J, DeVoss J, et al. Activity of tumor-associated macrophage depletion by CSF1R blockade is highly dependent on the tumor model and timing of treatment. *Cancer Immunol Immunother* 2021;**70**:2401−10.
27. Pello OM, De Pizzol M, Mirolo M, Soucek L, Zammataro L, Amabile A, et al. Role of c-MYC in alternative activation of human macrophages and tumor-associated macrophage biology. *Blood* 2012;**119**:411−21.
28. Li L, Ng D, Mah W, Almeida F, Rahmat S, Rao V, et al. A unique role for p53 in the regulation of M2 macrophage polarization. *Cell Death Differ* 2015;**22**:1081−93.
29. Zhong L, Zhang Y, Li M, Song Y, Liu D, Yang X, et al. E3 ligase FBXW7 restricts M2-like tumor-associated macrophage polarization by targeting c-Myc. *Aging (Albany NY)* 2020;**12**:24394.
30. Molina DM, Jafari R, Ignatushchenko M, Seki T, Larsson EA, Dan C, et al. Monitoring drug target engagement in cells and tissues using the cellular thermal shift assay. *Science* 2013;**341**:84−7.
31. Truica MI, Burns MC, Han H, Abdulkadir SA. Turning up the heat on MYC: progress in small-molecule inhibitors. *Cancer Res* 2021;**81**:248−53.
32. Dong H, Wu M, Wang Y, Du W, He Y, Shi Z. Total syntheses and anti-inflammatory activities of syringin and its natural analogues. *J Nat Prod* 2021;**84**:2866−74.
33. Luo P, Liu D, Zhang Q, Yang F, Wong YK, Xia F, et al. Celastrol induces ferroptosis in activated HSCs to ameliorate hepatic fibrosis *via* targeting peroxiredoxins and HO-1. *Acta Pharm Sin B* 2022;**12**:2300−14.
34. Seim GL, John SV, Arp NL, Fang Z, Pagliarini DJ, Fan J. Nitric oxide-driven modifications of lipoic arm inhibit α-ketoacid dehydrogenases. *Nat Chem Biol* 2023;**19**:265−74.
35. Wang N, Lu S, Cao Z, Li H, Xu J, Zhou Q, et al. Pyruvate metabolism enzyme DLAT promotes tumorigenesis by suppressing leucine catabolism. *Cell Metab* 2025;**37**:1381-99.e9.
36. Xie D-k, Yao J, Li P-h, Zhu Y-w, Chen J-n, Cao X-l, et al. Phenotypic comparison and the potential antitumor function of immortalized bone marrow-derived macrophages (iBMDMs). *Front Immunol* 2024;**15**:1379853.
37. Sung PS. Crosstalk between tumor-associated macrophages and neighboring cells in hepatocellular carcinoma. *Clin Mol Hepatol* 2021;**28**:333.
38. Zhang H, Liu L, Liu J, Dang P, Hu S, Yuan W, et al. Roles of tumor-associated macrophages in anti-PD-1/PD-L1 immunotherapy for solid cancers. *Mol Cancer* 2023;**22**:58.
39. Casey SC, Tong L, Li Y, Do R, Walz S, Fitzgerald KN, et al. MYC regulates the antitumor immune response through CD47 and PD-L1. *Science* 2016;**352**:227−31.

40. Dhanasekaran R, Hansen AS, Park J, Lemaitre L, Lai I, Adeniji N, et al. MYC overexpression drives immune evasion in hepatocellular carcinoma that is reversible through restoration of proinflammatory macrophages. *Cancer Res* 2023;**83**:626−40.
41. Zhu Y, Chen M, Xu D, Li TE, Zhang Z, Li JH, et al. The combination of PD-1 blockade with interferon-α has a synergistic effect on hepatocellular carcinoma. *Cell Mol Immunol* 2022;**19**:726−37.
42. Li H, Li X, Liu S, Guo L, Zhang B, Zhang J, et al. Programmed cell death-1 (PD-1) checkpoint blockade in combination with a mammalian target of rapamycin inhibitor restrains hepatocellular carcinoma growth induced by hepatoma cell−intrinsic PD-1. *Hepatology* 2017;**66**:1920−33.
43. Lau KM, Yue GGL, Chan YY, Kwok HF, Gao S, Wong CW, et al. A review on the immunomodulatory activity of Acanthopanax senticosus and its active components. *Chin Med* 2019;**14**:1−6.
44. Fu Z, Fan X, Wang X, Gao X. Cistanches Herba: an overview of its chemistry, pharmacology, and pharmacokinetics property. *J Ethnopharmacol* 2018;**219**:233−47.
45. Wu L, Georgiev MI, Cao H, Nahar L, El-Seedi HR, Sarker SD, et al. Therapeutic potential of phenylethanoid glycosides: a systematic review. *Med Res Rev* 2020;**40**:2605−49.
46. Arshad L, Haque MA, Harikrishnan H, Ibrahim S, Jantan I. Syringin from Tinospora crispa downregulates pro-inflammatory mediator production through MyD88-dependent pathways in lipopolysaccharide (LPS)-induced U937 macrophages. *Mol Biol Rep* 2024;**51**:789.
47. Cong S, Wang N, Pei H, Li Z, Meng Y, Maimaitituersun S, et al. Syringin inhibits the crosstalk between macrophages and fibroblast-like synoviocytes to treat rheumatoid arthritis *via* PDE4. *Phytomedicine* 2025;**138**:156401.
48. Zhao D, Liu K, Wang J, Shao H. Syringin exerts anti-inflammatory and antioxidant effects by regulating SIRT1 signaling in rat and cell models of acute myocardial infarction. *Immun Inflamm Dis* 2023;**11**:e775.
49. Liu Y, Zhu X, Tong X, Tan Z. Syringin protects against cerebral ischemia/reperfusion injury *via* inhibiting neuroinflammation and TLR4 signaling. *Perfusion* 2022;**37**:562−9.
50. Zhang H, Gu H, Jia Q, Zhao Y, Li H, Shen S, et al. Syringin protects against colitis by ameliorating inflammation. *Arch Biochem Biophys* 2020;**680**:108242.
51. Filipek A, Sadowska A, Skłodowska M, Muskała M, Czepielewska E. Syringin and phillygenin—natural compounds with a potential role in preventing lipid deposition in macrophages in the context of human atherosclerotic plaque. *Int J Mol Sci* 2025;**26**:6444.
52. Zhao C, Li P, Shi J, Cao S, Guo Y, Li G, et al. Curcumin ameliorates metabolic dysfunction-associated steatotic liver disease *via* targeting triokinase/FMN cyclase to regulate the expression of glycerol-3-phosphate acyltransferase 3: integration of chemical proteomics and transcriptomics. *Acta Pharm Sin B* 2026. Available from: https://doi.org/10.1016/j.apsb.2026.01.038.
53. Chen C, Zhu T, Liu X, Zhu D, Zhang Y, Wu S, et al. Identification of a novel PHGDH covalent inhibitor by chemical proteomics and phenotypic profiling. *Acta Pharm Sin B* 2022;**12**:246−61.
54. Sura MB, Zhou Y, Li J, Cheng Y. Discovery of papyifuran A as an unusual cembrane diterpenoid from *Boswellia papyrifera* resin reveals EEF2 as a potent new drug target for fibrosis of multiple organs. *Acta Pharm Sin B* 2025;**15**:3181−95.
55. Yu Z, Li Y, Li Y, Zhang J, Li M, Ji L, et al. Bufalin stimulates antitumor immune response by driving tumor-infiltrating macrophage toward M1 phenotype in hepatocellular carcinoma. *J Immunother Cancer* 2022;**10**:e004297.
56. Yang J, Xing Z. Ligustilide counteracts carcinogenesis and hepatocellular carcinoma cell-evoked macrophage M2 polarization by regulating yes-associated protein-mediated interleukin-6 secretion. *Exp Biol Med (Maywood)* 2021;**246**:1928−37.
57. Ou DL, Chen CW, Hsu CL, Chung CH, Feng ZR, Lee BS, et al. Regorafenib enhances antitumor immunity *via* inhibition of p38 kinase/Creb1/Klf4 axis in tumor-associated macrophages. *J Immunother Cancer* 2021;**9**:e001657.
58. Langston PK, Shibata M, Horng T. Metabolism supports macrophage activation. *Front Immunol* 2017;**8**:61.
59. Yang S, Zhang J, Xu Y, Wang J, Zhao H, Lei J, et al. OIT3 mediates macrophage polarization and facilitates hepatocellular carcinoma progression. *Cancer Immunol Immunother* 2022;**71**:2677−89.
60. Wang C, Zhang J, Yin J, Gan Y, Xu S, Gu Y, et al. Alternative approaches to target Myc for cancer treatment. *Signal Transduct Target Ther* 2021;**6**:117.
61. Bae S, Lee MJ, Mun SH, Giannopoulou EG, Yong-Gonzalez V, Cross JR, et al. MYC-dependent oxidative metabolism regulates osteoclastogenesis *via* nuclear receptor ERRα. *J Clin Investig* 2017;**127**:2555−68.
62. Purhonen J, Klefström J, Kallijärvi J. MYC—an emerging player in mitochondrial diseases. *Front Cell Dev Biol* 2023;**11**:1257651.
63. Jaynes JM, Sable R, Ronzetti M, Bautista W, Knotts Z, Abisoye-Ogunniyan A, et al. Mannose receptor (CD206) activation in tumor-associated macrophages enhances adaptive and innate antitumor immune responses. *Sci Transl Med* 2020;**12**:eaax6337.
64. Dhanasekaran R, Deutzmann A, Mahauad-Fernandez WD, Hansen AS, Gouw AM, Felsher DW. The MYC oncogene—the grand orchestrator of cancer growth and immune evasion. *Nat Rev Clin Oncol* 2022;**19**:23−36.
65. Stengel S, Petrie KR, Sbirkov Y, Stanko C, Ghazvini Zadegan F, Gil V, et al. Suppression of MYC by PI3K/AKT/mTOR pathway inhibition in combination with all-trans retinoic acid treatment for therapeutic gain in acute myeloid leukaemia. *Br J Haematol* 2022;**198**:338−48.
66. Harrington CT, Sotillo E, Dang CV, Thomas-Tikhonenko A. Tilting MYC toward cancer cell death. *Trends Cancer* 2021;**7**:982−94.
67. Zhang Y, Rao Y, Lu J, Wang J, Ker DFE, Zhou J, et al. The influence of biophysical niche on tumor-associated macrophages in liver cancer. *Hepatol Commun* 2024;**8**:e0569.
68. Ye Y, Xu Y, Lai Y, He W, Li Y, Wang R, et al. Long non-coding RNA cox-2 prevents immune evasion and metastasis of hepatocellular carcinoma by altering M1/M2 macrophage polarization. *J Cell Biochem* 2018;**119**:2951−63.
69. Arvanitakis K, Koletsa T, Mitroulis I, Germanidis G. Tumor-associated macrophages in hepatocellular carcinoma pathogenesis, prognosis and therapy. *Cancers (Basel)* 2022;**14**:226.
70. Huang J, Wu Q, Geller DA, Yan Y. Macrophage metabolism, phenotype, function, and therapy in hepatocellular carcinoma (HCC). *J Transl Med* 2023;**21**:815.
71. Qiu X, Zhou T, Li S, Wu J, Tang J, Ma G, et al. Spatial single-cell protein landscape reveals vimentinhigh macrophages as immune-suppressive in the microenvironment of hepatocellular carcinoma. *Nat Cancer* 2024;**5**:1557−78.